International Journal of Solids and Structures xxx (xxxx) xxx

Contents lists available at ScienceDirect

International Journal of Solids and Structures

journal homepage: www.elsevier.com/locate/ijsolstr

A unified dual modeling framework for soft and hard magnetorheological elastomers

Dipayan Mukherjee [a,*], Kostas Danas [b,*]

[a] Department of Engineering, University of Cambridge, CB2 1PZ, UK
[b] LMS, C.N.R.S, École Polytechnique, Institut Polytechnique de Paris, Palaiseau, 91128, France

ARTICLE INFO

Keywords:
Magnetoelasticity
Finite strains
Magnetorheological elastomers
Finite elasticity
Constitutive modeling

ABSTRACT

Most current magnetorheological elastomers (MREs) are broadly categorized into hard (*h*-MREs) and soft (*s*-MREs) depending on the magnetic properties of the underlying particles. The former consist of particles exhibiting strong magnetic dissipation (e.g., NdFeB), while the latter are purely energetic (e.g., carbonyl iron). In this work, we present a unified modeling framework for *h*-MREs including the response of the *s*-MREs as a limiting case when the dissipation is set to zero. In addition, the proposed framework is dual in the sense of a partial Legendre–Fenchel transform of the magnetic part, i.e., we propose exactly equivalent models in the $\mathbf{F}-\mathbf{H}$ and $\mathbf{F}-\mathbf{B}$ variable spaces. Efficient finite element, numerical solutions for various boundary value problems (BVPs) involving *h*- and *s*-MREs are obtained via incremental variational principles. The calculations for the end-tip deflection of a uniformly pre-magnetized cantilever exhibit excellent agreement with the experimental data. The investigations on the remanent fields and the magnetic actuation performance of hybrid *h*-/*s*-MRE rank-1 laminated cantilevers and non-uniformly pre-magnetized, functionally graded beams are also carried out. The analysis shows that pre-magnetization profiling of the *h*-MRE beams allows to program efficiently the deflection patterns upon subsequent application of a small actuating magnetic field. Furthermore, concentrating the hard-magnetic particles near the beam flanks reduces the actuation field considerably. The proposed $\mathbf{F}-\mathbf{H}$ and $\mathbf{F}-\mathbf{B}$-based modeling frameworks and their numerical implementations serve as useful tools in analyzing the magneto-mechanical performance of the MRE structures made of *s*- and *h*-MREs.

1. Introduction

Recent advances in the manufacturing of particle-filled magnetorheological elastomers (MREs) via 3D printing (Wang et al., 2019; Zhou et al., 2020) and advanced curing techniques (Zhao et al., 2019; Ren et al., 2019; Alapan et al., 2020) uncover a vast range of opportunities towards designing programmable shape changing materials and soft robotic manipulators (see the recent review articles by Bira et al. (2020), Bastola and Hossain (2021) and Lucarini et al. (2022)). Depending on the magnetic properties (e.g., coercivity, remanence, etc.) of the underlying magneto-active particles, the MRE composites are broadly classified into two categories, namely "soft" and "hard" MREs (or *s*-MRE and *h*-MRE in short). Moreover, recent works by Linke et al. (2016) also investigate the performance of the "hybrid" MREs containing both the soft and hard magnetic particles.

Magnetically soft particles, e.g., iron, exhibit negligible hysteresis loss and demagnetize completely after the removal of the external magnetic field (Bodelot et al., 2017). The hard magnets, on the other hand, exhibit ferromagnetic hysteresis and thus *do not* de-magnetize after removal of the external magnetic field (Linnemann et al., 2009; Mukherjee and Danas, 2019). This residual magnetic field in the particles is typically termed as the "remanent" magnetic field. In fact, the commercially-available, hard-magnetic NdFeB particles of ∼5–20 μm diameter (commercially known as the MQP particles) exhibit considerable amount of magnetic remanence, and thus, serves as an excellent candidate in the fabrication of *h*-MREs.

The continuum magneto-elastic modeling considering small strains traces its way back to Brown (1966). Later, Pao and Hutter (1975) extended this small strain frameworks and incorporated the state-dependent internal variables in the thermodynamic framework. The finite-strain magneto-elastic modeling framework, specifically for the *s*-MREs has been first proposed by Dorfmann and Ogden (2003, 2004) and Kankanala and Triantafyllidis (2004). A number of phenomenological constitutive models for the *s*-MREs have been proposed during the subsequent years. However, a continuum modeling framework for the dissipative *h*-MREs has been proposed only recently. Furthermore, in the general sense, the complete dissipative *h*-MRE modeling includes

* Corresponding authors.
E-mail addresses: dm914@cam.ac.uk (D. Mukherjee), konstantinos.danas@polytechnique.edu (K. Danas).

https://doi.org/10.1016/j.ijsolstr.2022.111513
Received 12 November 2021; Received in revised form 22 January 2022; Accepted 10 February 2022
Available online 23 February 2022

Please cite this article as: Dipayan Mukherjee, Kostas Danas, *International Journal of Solids and Structures*, https://doi.org/10.1016/j.ijsolstr.2022.111513

the *s*-MRE as a limiting case; that of vanishing dissipation. This work attempts to establish a complete unified framework in this regard for both *s*- and *h*-MREs.

Currently, depending on the modeling approach, the continuum models for the *s*- and *h*-MREs may be broadly categorized into four classes, namely, (i) phenomenological continuum models, (ii) variational homogenization-based models, (iii) homogenization-guided phenomenological models and (iv) decoupled reduced-order models for slender structures. As the name suggests, the last in this list is not a full continuum model that is independent of the geometry. Thus, classifying them in the same "continuum modeling" hierarchy may be debatable.

(i) Phenomenological continuum models: The phenomenological, finite strain magneto-elastic models are typically expressed in terms of a number of material parameters, which need to be calibrated against experimental or numerical data (Kankanala and Triantafyllidis, 2004; Dorfmann and Ogden, 2004, 2005; Danas et al., 2012). In fact, such phenomenological models for *s*-MREs are closed-form and thus straightforward to implement in a fully implicit finite element (FE) solver routine and thus, are typically employed in the structural deflections and instability analysis involving such materials (Danas and Triantafyllidis, 2014; Keip and Rambausek, 2016, 2017; Psarra et al., 2017, 2019).

The numerical implementation of the fully nonlinear, coupled phenomenological models for magneto/electro-active elastomers are indeed involved. In this regard we refer the works of Miehe et al. (2011), Rosato and Miehe (2014), Ethiraj and Miehe (2016) providing efficient finite-element-based numerical computation algorithms for the active materials.

(ii) Homogenization-based models: The analytical homogenization-based models for the *s*-MREs based on the "variational" homogenization (Ponte Castañda and Galipeau, 2011; Galipeau and Ponte Castañda, 2013) and the "differential" homogenization (Lefère and Lopez-Pamies, 2017) approaches typically provide an effective strain energy density in terms of the properties of the underlying constituents and that of the representative volume element (RVE). However, in contrast to the phenomenological models, the homogenization-based models are usually implicit, i.e., require a set of additional differential/algebraic constraint equations to be solved in order to extract the local constitutive response. As a result, this complicates the evaluation of the jacobian matrix and usually leads to difficult convergence. Consequently, the numerical realization of these models in a fully implicit FE setting becomes notoriously difficult. Besides the analytical homogenization estimates, full field numerical homogenization estimates for the *s*- (Danas, 2017; Rambausek and Keip, 2018; Mukherjee et al., 2020) and *h*- (Kalina et al., 2017; Mukherjee et al., 2021) MREs have also been investigated. However, the numerical homogenization poses several challenges regarding applying a background magnetic field and extracting the effective magnetostriction responses. These issues can be addressed by suitably augmenting the variational principle for the numerical homogenization computations (Danas, 2017). In any case, those analytical and numerical homogenization models include important microstructural information (e.g., the particle volume fraction or their distributions) and thus can serve as important test-models to inform, derive and calibrate the previously phenomenological models. In this class of materials, recently Garcia-Gonzalez and Hossain (2020) have proposed models based on dipole interactions. Those models are explicit and require a number of terms to resolve the particle interactions. To keep the number of terms low, simpler periodic lattice microstructures were considered (such as FCC or BCC type) showing very promising capabilities. Yet, those simpler periodic distributions are not isotropic, while it is not clear if they are able to reproduce accurately long-range, loss-of-ellipticity and bifurcation effects such as those described in particle-chain microstructures (Danas and Triantafyllidis, 2014), since they are based on nearest-neighbor, particle interactions.

(iii) Homogenization-guided phenomenological models: To avoid the difficulties associated with the phenomenological and homogenization models, a set of recent works propose a "homogenization-guided" modeling approach for the soft (Mukherjee et al., 2020; Lefèvre and Lopez-Pamies, 2020) and hard (Mukherjee et al., 2021) MREs. These models are proposed in such a way that they yield the rigorous analytical homogenization estimates under several limiting conditions, while remaining explicit similar to the purely phenomenological ones. Consequently, such a modeling strategy drastically reduces the number of calibration parameters, which are then evaluated by comparing the local model response with the corresponding analytical and/or numerical homogenization responses. Moreover, these explicit models can be directly implemented in a fully implicit FE solver to compute the structural responses of the soft (Rambausek and Danas, 2021; Dorn et al., 2021) and hard (Mukherjee et al., 2021) MRE-based structures under externally applied magnetic and mechanical fields.

(iv) Reduced-order models: The decoupled, reduced-order models are specifically of interest for the pre-magnetized, slender *h*-MRE structures (Kim et al., 2018; Zhao et al., 2019; Garcia-Gonzalez, 2019; Wang et al., 2020, 2021; Yan et al., 2021a). These class of models, which are directly inspired by numerous earlier torque-type models (see for instance the monograph of Brown (1966) for magnetized bodies as well as some earlier (Yih-Hsing and Chau-Shioung, 1973) and Lum et al. (2016) and more recent (Abbott et al., 2007; Gerbal et al., 2015) models), are distinctly different from the last three classes of *s*- and *h*-MRE models in the sense that they involve no "intrinsic" magnetomechanical coupling, no magnetic dissipation (and thus are valid for small applied magnetic fields) and require the knowledge of the pre-magnetized state. Yet, these reduced-order models facilitate straightforward numerical computations for the pre-magnetized beams and thus, are particularly of interest in designing soft robotic slender devices (Zhao et al., 2019; Wang et al., 2021). However, it is noted that the key reduced-order modeling assumption of spatially uniform magnetic fields (Wang et al., 2020; Yan et al., 2021a) may become increasingly inaccurate when the orientation of the pre-magnetization field varies along the beam's length (Mukherjee et al., 2021). In that case, the non-uniform pre-magnetization profile needs to be considered explicitly (Yan et al., 2021a).

All the aforementioned finite-strain modeling frameworks consider either a scalar potential-based $\mathbf{F}-\mathbf{H}$ (Lefère and Lopez-Pamies, 2017; Lefèvre and Lopez-Pamies, 2020; Mukherjee et al., 2021) or a vector potential-based $\mathbf{F}-\mathbf{B}$ (Dorfmann and Ogden, 2004, 2005; Kankanala and Triantafyllidis, 2004; Danas, 2017) formulation. In fact, the scalar and vector potential-based models have distinct advantages over one another. For example, being based on a scalar potential (i.e. one additional degree of freedom), the $\mathbf{F}-\mathbf{H}$ models allow for a time-efficient numerical computation schemes (Javili et al., 2013; Mukherjee et al., 2020). The $\mathbf{F}-\mathbf{B}$ models, on the other hand, include three additional degrees of freedom thus increasing the time cost of simulations but instead are based on a minimization variational principle. Thus, the structural stability analysis using the $\mathbf{F}-\mathbf{B}$ model becomes advantageous since one can directly attribute the loss of positive definiteness of the global stiffness matrix to the bifurcation point (Psarra et al., 2017, 2019; Rambausek and Danas, 2021; Polukhov and Keip, 2021). In addition, in a number of practical device-based applications (Dorn et al., 2021), where actual coils need to be modeled, the $\mathbf{F}-\mathbf{B}$ models are a natural choice since the electric currents are physically conjugate to the magnetic vector potential. Evidently, one may employ, in theory, a partial Legendre–Fenchel transformation to obtain the $\mathbf{F}-\mathbf{B}$ model energy densities from the $\mathbf{F}-\mathbf{H}$ model or vice-versa (Bustamante et al., 2008), but in numerous cases such an operation is not analytical due to the non-linearity of the constitutive terms.

The objective of this paper is thus twofold. First, we develop dual (in magnetic terms) $\mathbf{F}-\mathbf{H}$ and $\mathbf{F}-\mathbf{B}$-based continuum formulations for general, dissipative *h*-MREs and second, we show that a *s*-MRE model may be readily obtained as a special case of the *h*-MRE ones in the limit of vanishing dissipation. In this view, a single continuum model becomes sufficient to model both *h*- and *s*-MREs in a fully consistent

manner. To accomplish that, we first derive the variational principles and derive the local (point wise) constitutive laws for the $\mathbf{F}-\mathbf{H}$ and $\mathbf{F}-\mathbf{B}$ models in a Lagrangian setting in Section 2. Next, specific constitutive choices for the energy densities and dissipation potentials are provided in Section 3. Specifically, in this section, we use the recent $\mathbf{F}-\mathbf{H}$ model of Mukherjee et al. (2021) for the *h*-MREs to derive its dual $\mathbf{F}-\mathbf{B}$ model energy densities via a partial Legendre–Fenchel transform. The model calibration is carried out subsequently in Section 4, where a coupling parameter is evaluated by fitting the $\mathbf{F}-\mathbf{H}$ model response with full-field numerical homogenization results. The local magnetization and magnetostriction responses for the *h*- and *s*-MREs, emerging from both, $\mathbf{F}-\mathbf{H}$ and $\mathbf{F}-\mathbf{B}$ models are shown therein. We subsequently employ the scalar potential-based $\mathbf{F}-\mathbf{H}$ and the vector potential-based $\mathbf{F}-\mathbf{B}$ models for the solution of structural boundary value problems (BVPs) involving slender structures. Specific details on the remote application of the magnetic fields and modeling of the surrounding air are discussed in Section 5. Next, we solve BVPs involving uniformly pre-magnetized *h*-MRE, *s*-MRE and hybrid *h*-/*s*-MRE cantilever beams as well as some combinations of non-uniformly pre-magnetized, functionally-graded *h*-MRE beams in Section 6. Finally, we conclude by discussing the key features of the proposed models and the implications of the numerically computed results.

2. Variational framework and constitutive relations

We consider a deformable, magneto-active solid in $\mathbb{R}^3$ occupying a volume $\mathcal{V}_0$ ($\mathcal{V}$) in its reference (current) configuration. The boundary of the solid is designated by $\partial\mathcal{V}_0$ ($\partial\mathcal{V}$), while $\mathcal{N}$ ($\mathbf{n}$) denotes the unit normal on $\partial\mathcal{V}_0$ ($\partial\mathcal{V}$) in the reference (current) configuration (see Fig. 1a). The deformation of the solid from the reference to current configuration is defined to be a continuous, twice differentiable (except on the boundary/interfaces), one-to-one mapping $\mathbf{y}(\mathbf{X})$. Thus, the position of any point $\mathbf{X}$ in the reference configuration is given by $\mathbf{x}=\mathbf{y}(\mathbf{X})$ in the current configuration. The deformation gradient is then defined to be $\mathbf{F}=\text{Grad}\,\mathbf{y}$, along with $J=\det\mathbf{F}>0$. Furthermore, the mechanical displacement field $\mathbf{u}(\mathbf{X})$ relates the current position vector to the reference so that $\mathbf{x}=\mathbf{X}+\mathbf{u}(\mathbf{X})$. Consequently, $\mathbf{F}$ relates to $\mathbf{u}$ via $\mathbf{F}=\mathbf{I}+\text{Grad}\,\mathbf{u}$, where $\mathbf{I}$ is the second-order identity tensor.

Next, we derive the governing equations for the primary and internal variables in a Lagrangian setting from an augmented energy rate functional, which is described in terms of the rate of the stored potential energy and dissipation potential. First, the scalar potential-based $\mathbf{F}-\mathbf{H}$ formulation is presented. It would be followed by the vector potential-based $\mathbf{F}-\mathbf{B}$ formulation. Throughout the paper, we consider quasi-static mechanical deformations under no mechanical body force (although this last may be added to solve a BVP (Dorn et al., 2021)). Moreover, no free space charge or electrical current are considered in the analysis.

2.1. Scalar potential-based $\mathbf{F}-\mathbf{H}$ formulation

We consider the mechanical deformation $\mathbf{u}$ and the scalar magnetic potential φ to be the independent primary variables along with a vector internal variable $\boldsymbol{\xi}$. Notice that under no spatial current density and electric field, the local (point wise) Ampere's law reads $\text{Curl}\,\mathbf{H}=\mathbf{0}$, which, in turn, allows us to express $\mathbf{H}$ in terms of the gradient of a scalar potential, so that $\mathbf{H}=-\text{Grad}\varphi$. Having said that, the rate of the potential energy stored in the system, shown in Fig. 1a, reads

$$\dot{\mathscr{P}}^{\text{H}}=\frac{\text{d}}{\text{d}t}\int_{\mathbb{R}^3}W^{\text{H}}(\mathbb{C},\mathbf{H},\boldsymbol{\xi})\,\text{d}\mathcal{V}_0-\int_{\partial\mathcal{V}_0}\mathbf{T}\cdot\dot{\mathbf{u}}\,\text{d}S_0. \tag{2.1}$$

Here, $W^{\text{H}}(\mathbb{C},\mathbf{H},\boldsymbol{\xi})$ is the local potential energy density, where $\mathbb{C}=\mathbf{F}^T\mathbf{F}$ is the right Cauchy–Green tensor and $\mathbf{T}$ is the mechanical traction on the boundary $\partial\mathcal{V}_0$. The operators ($\dot{\blacksquare}$) and $\text{d}/\text{d}t$ in (2.1) denote the material time derivative. Notice that the local energy density $W^{\text{H}}(\mathbf{F},\mathbf{H},\boldsymbol{\xi})$ is non-zero not only in $\mathcal{V}_0$ but also in $\mathbb{R}^3\setminus\mathcal{V}_0$, which is typical in the magneto-mechanical formulation (Kankanala and Triantafyllidis, 2004).

The dissipation potential $\mathscr{D}$ associated with the solid is also given in terms of the local dissipation potential $D(\dot{\boldsymbol{\xi}})$, such that

$$\mathscr{D}=\int_{\mathcal{V}_0}D(\dot{\boldsymbol{\xi}})\,\text{d}\mathcal{V}_0. \tag{2.2}$$

Notice that the dissipation is only considered in the *h*-MRE, whereas $D(\dot{\boldsymbol{\xi}})$ vanishes identically for all $\mathbf{X}\in\mathbb{R}^3\setminus\mathcal{V}_0$. With these, we propose a variational principle following the seminal works of Onsager (1931a,b), so that

$$\dot{\Pi}^{\text{H}}=\inf_{\dot{\mathbf{u}}\in\widetilde{\mathcal{U}}}\sup_{\dot{\varphi}\in\widetilde{\mathcal{G}}}\inf_{\dot{\boldsymbol{\xi}}\in\mathbb{R}^3}\left[\dot{\mathscr{P}}^{\text{H}}+\mathscr{D}\right]. \tag{2.3}$$

The admissible sets for $\dot{\mathbf{u}}$ and $\dot{\varphi}$ are given by

$$\widetilde{\mathcal{U}}\equiv\left\{\dot{\mathbf{u}}(\mathbf{X}):\dot{\mathbf{F}}(\mathbf{X})=\text{Grad}\,\dot{\mathbf{u}}(\mathbf{X})\ \ \forall\,\mathbf{X}\in\mathbb{R}^3,\ \text{ and }\ \pi(\dot{\mathbf{u}}(\mathbf{X}))=\pi(\bar{\dot{\mathbf{u}}}(\mathbf{X}))\ \ \forall\,\mathbf{X}\in\partial\mathcal{V}_0^{\mathbf{u}}\right\} \tag{2.4}$$

and

$$\widetilde{\mathcal{G}}\equiv\left\{\dot{\varphi}(\mathbf{X}):\dot{\mathbf{H}}(\mathbf{X})=-\text{Grad}\,\dot{\varphi}(\mathbf{X})\ \ \forall\,\mathbf{X}\in\mathbb{R}^3,\ \text{ and }\ \dot{\varphi}(\mathbf{X})=\bar{\dot{\varphi}}(\mathbf{X})\ \ \forall\,\mathbf{X}\in\partial\mathcal{V}_\infty^{\varphi}\right\}, \tag{2.5}$$

respectively. The operator π in (2.4) denotes a projection operator that enables applying the constraints only on the certain components on $\dot{\mathbf{u}}$ for all $\mathbf{X}$ on the MRE boundary $\partial\mathcal{V}_0^{\mathbf{u}}$, where the displacement is constrained to vary with a reference rate $\bar{\dot{\mathbf{u}}}$. Similarly, the boundary where the magnetic potential φ varies according to a given rate $\bar{\dot{\varphi}}$ is denoted as $\partial\mathcal{V}_\infty^{\varphi}$. Since the magnetic fields are typically applied far away from the *h*-MRE sample, we consider $\partial\mathcal{V}_\infty^{\varphi}$ to be an interface far away from the *h*-MRE boundary $\partial\mathcal{V}_0$. However, this particular consideration does *not* affect the generality of the variational principle (2.3).

The stationarity conditions for $\dot{\Pi}^{\text{H}}$ along with the arbitrariness of the considered volume element in $\mathcal{V}_0$ leads to the local governing equations and the boundary conditions in this scalar potential formulation. Thus, straightforward algebraic manipulations (see Kankanala and Triantafyllidis (2004) or Bustamante et al. (2008) for instance) leads to

$$\text{Div}\,\mathbf{S}=\mathbf{0}\ \ \text{in}\ \ \mathbb{R}^3,\qquad\text{with}\ \ \mathbf{S}=2\mathbf{F}\frac{\partial W^{\text{H}}}{\partial\mathbb{C}}\qquad\text{and}$$

$$[\![\mathbf{S}]\!]\cdot\mathcal{N}-\mathbf{T}=\mathbf{0}\ \ \text{on}\ \ \partial\mathcal{V}_0\setminus\partial\mathcal{V}_0^{\mathbf{u}}, \tag{2.6}$$

$$\text{Div}\,\mathbf{B}=0\ \ \text{in}\ \ \mathbb{R}^3,\qquad\text{with}\ \ \mathbf{B}=-\frac{\partial W^{\text{H}}}{\partial\mathbf{H}}\qquad\text{and}$$

$$[\![\mathbf{B}]\!]\cdot\mathcal{N}=0\ \ \text{on}\ \ \partial\mathcal{V}_0, \tag{2.7}$$

$$\frac{\partial W^{\text{H}}}{\partial\boldsymbol{\xi}}+\frac{\partial D}{\partial\dot{\boldsymbol{\xi}}}=\mathbf{0}\ \ \text{for all}\ \ \mathbf{X}\in\mathcal{V}_0,\qquad\text{with}\qquad\boldsymbol{\eta}=\frac{\partial D}{\partial\dot{\boldsymbol{\xi}}}=-\frac{\partial W^{\text{H}}}{\partial\boldsymbol{\xi}}. \tag{2.8}$$

Here, $\boldsymbol{\eta}$ is the work conjugate of the internal variable $\boldsymbol{\xi}$. Equations $(2.6)_1$ and $(2.6)_2$ represent, respectively, the local balance law and constitutive relation for the first Piola–Kirchhoff stress $\mathbf{S}$, whereas, $(2.6)_3$ represents the jump condition for $\mathbf{S}$ at the *h*-MRE/Air boundary $\partial\mathcal{V}_0$. Similarly, the balance law, constitutive definition and the boundary condition for $\mathbf{B}$ is given in (2.7). Finally, the variational principle also leads to the generalized standard materials (Halphen and Son Nguyen, 1975) relation $(2.8)_1$, which is, in fact, the local evolution equation for the internal variable $\boldsymbol{\xi}$. Notice that unlike the primary variables $\mathbf{u}$ and φ, the internal variable $\boldsymbol{\xi}$ *does not* need to satisfy any differential or boundary constraints. Moreover, the evolution equation $(2.8)_1$ only holds in the *h*-MRE domain, i.e., for all $\mathbf{X}\in\mathcal{V}_0$.

Entropy imbalance and constraint on $D(\dot{\boldsymbol{\xi}})$: The local form of the entropy imbalance equation, also known as the Clausius–Duhem inequality reads for the $\mathbf{F}-\mathbf{H}$ model (Mukherjee, 2020; Mukherjee et al., 2021)

$$\mathbf{S}:\dot{\mathbf{F}}-\mathbf{B}\cdot\dot{\mathbf{H}}-\dot{W}^{\text{H}}(\mathbb{C},\mathbf{H},\boldsymbol{\xi})\geq 0. \tag{2.9}$$

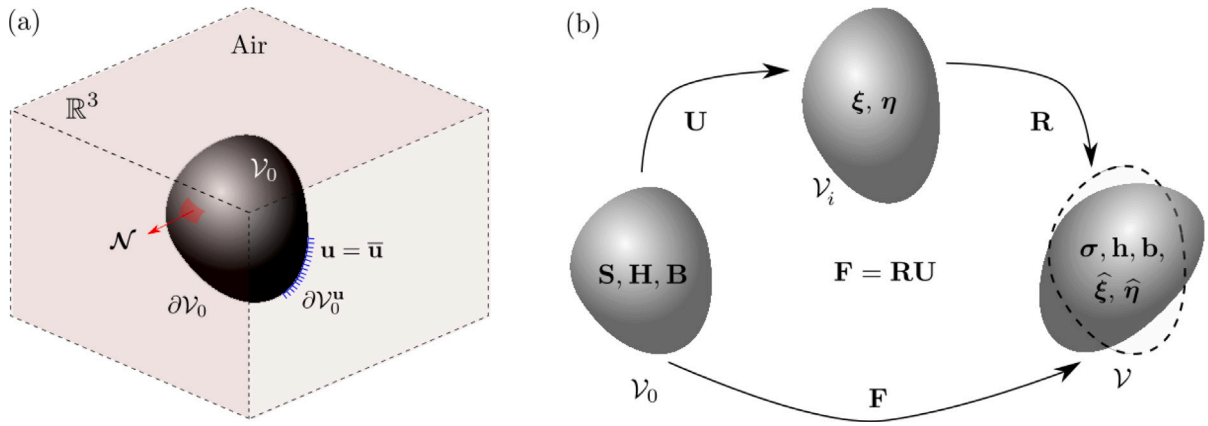

Fig. 1. (a) Reference configuration of the h-MRE of volume $\mathcal{V}_0$ and boundary $\partial\mathcal{V}_0$ along with the surrounding air, occupying a volume $\mathbb{R}^3 \setminus \mathcal{V}_0$. (b) Definition of the reference, intermediate and current configurations of volume $\mathcal{V}_0$, $\mathcal{V}_i$ and $\mathcal{V}$, respectively, along with the different field variables defined therein.

Expanding the derivative $\dot{W}^{\mathrm{H}}$ followed by substitutions of the constitutive relations $(2.6)_1$, $(2.7)_1$ and $(2.8)_1$ into (2.9) we obtain

$$\frac{\partial D}{\partial \dot{\boldsymbol{\xi}}} \cdot \dot{\boldsymbol{\xi}} \geq 0, \tag{2.10}$$

which is typically referred to be the dissipation inequality. Notably, any convex $D(\dot{\boldsymbol{\xi}})$ satisfies the dissipation inequality, ensuring a positive dissipation during any loading/unloading operation.

2.2. Vector potential-based $\mathbf{F} - \mathbf{B}$ formulation

Next, we derive the local balance laws and constitutive relations for an equivalent $\mathbf{F} - \mathbf{B}$-based formulation. Notice that, the $\mathbf{B}$ field is divergence-free and hence is now expressed in terms of a vector potential $\mathbf{A}$, so that $\mathbf{B} = \mathrm{Curl}\,\mathbf{A}$. In this formulation, we consider $\mathbf{u}$ and $\mathbf{A}$ to be the primary variables, while the internal variable remains the same, i.e., $\boldsymbol{\xi}$.

The rate of total potential energy is then given by

$$\begin{aligned} &\dot{\mathscr{P}}^{\mathrm{B}} = \frac{\mathrm{d}}{\mathrm{d}t}\int_{\mathbb{R}^3} W^{\mathrm{B}}(\mathbb{C}, \mathbf{B}, \boldsymbol{\xi})\, \mathrm{d}\mathcal{V}_0 - \int_{\partial\mathcal{V}_0} \mathbf{T}\cdot\dot{\mathbf{u}}\, \mathrm{d}S_0, \quad \text{with} \\ &W^{\mathrm{B}}(\mathbb{C}, \mathbf{B}, \boldsymbol{\xi}) = \sup_{\mathbf{H}}\Big[W^{\mathrm{H}}(\mathbb{C}, \mathbf{H}, \boldsymbol{\xi}) + \mathbf{H}\cdot\mathbf{B}\Big], \end{aligned} \tag{2.11}$$

which is the partial Legendre–Fenchel transform of $W^{\mathrm{H}}(\mathbb{C}, \mathbf{H}, \boldsymbol{\xi})$ with respect to $\mathbf{H}$ (Bustamante et al., 2008). The dissipation potential, which is defined only in terms of the rate of the internal variable $\dot{\boldsymbol{\xi}}$ is considered to be identical to the $\mathbf{F} - \mathbf{B}$ formulation as well. Thus, the minimization variational principle in terms of $\dot{\mathscr{P}}^{\mathrm{B}}$ and $\mathscr{D}$ now reads

$$\dot{\Pi}^{\mathrm{B}} = \inf_{\dot{\mathbf{u}}\in\widetilde{\mathcal{U}}} \inf_{\dot{\mathbf{A}}\in\widetilde{\mathcal{B}}} \inf_{\dot{\boldsymbol{\xi}}\in\mathbb{R}^3} \Big[\, \dot{\mathscr{P}}^{\mathrm{B}} + \mathscr{D} \,\Big], \tag{2.12}$$

where the admissible set $\widetilde{\mathcal{U}}$ for the rate $\dot{\mathbf{u}}$ is given by (2.4) and that for $\dot{\mathbf{A}}$ reads[1]

$$\widetilde{\mathcal{B}} \equiv \Big\{ \dot{\mathbf{A}}(\mathbf{X}) : \dot{\mathbf{B}}(\mathbf{X}) = \mathrm{Curl}\,\dot{\mathbf{A}}(\mathbf{X}) \;\; \forall\, \mathbf{X}\in\mathbb{R}^3, \;\; \text{and} \;\; \dot{\mathbf{A}}(\mathbf{X}) = \dot{\overline{\mathbf{A}}}(\mathbf{X}) \;\; \forall\, \mathbf{X}\in\partial\mathcal{V}_\infty^{\mathbf{A}} \Big\}, \tag{2.13}$$

where the specific rate $\dot{\overline{\mathbf{A}}}$ is considered on the boundary $\partial\mathcal{V}_\infty^{\mathbf{A}}$ that is far from the Air/MRE interface $\partial\mathcal{V}_0$.

[1] The numerical solution for the three-dimensional vector potential-based BVPs requires an additional constraint on $\mathbf{A}$, namely, $\mathrm{Div}\,\mathbf{A} = 0$, commonly referred as the Coulomb gauge. The latter is not necessary in two-dimensional problem. We include Coulomb gauge condition in the admissible set for $\mathbf{A}$ in Section 5, where further specialization of the rate-type variational principles towards numerical implementation is carried out.

Again, the minimizing $\dot{\Pi}^{\mathrm{B}}$ with respect to the rates $\dot{\mathbf{u}}$, $\dot{\mathbf{A}}$ and $\dot{\boldsymbol{\xi}}$ leads to the local balance laws, constitutive relations along with the boundary conditions, so that

$$\begin{aligned} &\mathrm{Div}\,\mathbf{S} = \mathbf{0} \quad \text{in} \quad \mathbb{R}^3, \quad \text{with} \quad \mathbf{S} = 2\mathbf{F}\frac{\partial W^{\mathrm{B}}}{\partial \mathbb{C}} \quad \text{and} \\ &[\![\mathbf{S}]\!]\cdot\mathcal{N} - \mathbf{T} = \mathbf{0} \quad \text{on} \quad \partial\mathcal{V}_0 \setminus \partial\mathcal{V}_0^{\mathbf{u}}, \end{aligned} \tag{2.14}$$

$$\mathrm{Curl}\,\mathbf{H} = \mathbf{0} \quad \text{in} \quad \mathbb{R}^3, \quad \text{with} \quad \mathbf{H} = \frac{\partial W^{\mathrm{B}}}{\partial \mathbf{B}} \quad \text{and}$$

$$\mathcal{N}\times[\![\mathbf{H}]\!] = \mathbf{0} \quad \text{on} \quad \partial\mathcal{V}_0, \tag{2.15}$$

$$\frac{\partial W^{\mathrm{B}}}{\partial \boldsymbol{\xi}} + \frac{\partial D}{\partial \dot{\boldsymbol{\xi}}} = \mathbf{0} \quad \text{for all} \quad \mathbf{X}\in\mathcal{V}_0, \quad \text{with} \quad \boldsymbol{\eta} = \frac{\partial D}{\partial \dot{\boldsymbol{\xi}}} = -\frac{\partial W^{\mathrm{B}}}{\partial \boldsymbol{\xi}}. \tag{2.16}$$

Notice that (2.14) and (2.16) remain identical to (2.6) and (2.8), respectively, with the only difference being the replacement of W^{H} with W^{B}. The minimization of $\dot{\Pi}^{\mathrm{B}}$ with respect to $\dot{\mathbf{A}}$ yields the local balance law $(2.15)_1$, constitutive relation $(2.15)_2$ and the interface/boundary condition $(2.15)_3$ on $\partial\mathcal{V}_0$.

The $\mathbf{F} - \mathbf{B}$ version of the local Clausius–Duhem inequality can be readily obtained by substituting $(2.11)_2$ into (2.9). Subsequently, the dissipation inequality can be derived *mutatis mutandis* the $\mathbf{F} - \mathbf{H}$ case. In fact, the final form of the dissipation inequality remains identical to (2.10), which is obvious since D remains independent of $\mathbf{H}$ or $\mathbf{B}$.

2.3. Current configuration representations of $\mathbf{S}$, $\mathbf{H}$, $\mathbf{B}$ and $\boldsymbol{\xi}$

Push forward transformations of $\mathbf{S}$, $\mathbf{H}$ *and* $\mathbf{B}$: A set of equivalent balance laws can be derived at the current configuration as well via the local mass-momentum-flux conservation considerations (Kankanala and Triantafyllidis, 2004; Dorfmann and Ogden, 2004). Of interest, in this work, is to express the current configuration stress and magnetic field quantities in terms of their referential counterparts and $\mathbf{F}$. Such expressions can be obtained directly from the equivalence of the balance laws in the reference and current configurations, so that

$$\boldsymbol{\sigma} = \frac{1}{J}\mathbf{S}\mathbf{F}^T, \qquad \mathbf{b} = \frac{1}{J}\mathbf{F}\mathbf{B} \qquad \text{and} \qquad \mathbf{h} = \mathbf{F}^{-T}\mathbf{H}, \tag{2.17}$$

where $\boldsymbol{\sigma}$ is the (total) Cauchy stress and $\mathbf{b}$, $\mathbf{h}$ are the current configuration equivalents of $\mathbf{B}$ and $\mathbf{H}$, respectively.

The current magnetization $\mathbf{m}$ can be subsequently obtained from the well-known constitutive relation

$$\mathbf{b} = \mu_0(\mathbf{h} + \mathbf{m}). \tag{2.18}$$

We note that some of the earlier works (Kankanala and Triantafyllidis, 2004; Danas et al., 2012) on the s-MREs also consider $\mathbf{m}$ to be the primary variable and therein, the $\mathbf{h}$ field is obtained as a dual variable from the $\mathbf{m}$-based free energy function. However, $\mathbf{m}$ is *not* subject to any differential/boundary constraint, which, in turn, necessitates an

additional unknown field, namely, the vector potential field $\mathbf{A}$ to be solved for in order to obtain a full numerical resolution of the coupled magneto-mechanical boundary value problem (BVP) (see Appendix A of Danas (2017) for details). Thus, here we refrain from a model proposition in terms of $\mathbf{m}$. Rather, this text considers $\mathbf{m}$ to be a *derived quantity* that is useful in the presentation and interpretation of the results.

Push forward transformation of $\boldsymbol{\xi}$: In addition to the push-forward transformations for the primary $\mathbf{H}$ (for $\mathbf{F}-\mathbf{H}$ model) and $\mathbf{B}$ (for $\mathbf{F}-\mathbf{B}$ model), the proposition for the push-forward transformation of the internal variable $\boldsymbol{\xi}$ is necessary to complete the independent variable definitions and their mappings between the different configurations. Since there is no differential or boundary constraint on $\boldsymbol{\xi}$, the proposition for its Eulerian counterpart $\widehat{\boldsymbol{\xi}}$ ends up being a mere *constitutive choice*. This choice, in turn, is made from the physical nature of the internal variable $\boldsymbol{\xi}$. As per the typical definitions of the "switching surface"-based ferromagnetic hysteresis theories (Bassiouny et al., 1988; Huber et al., 1999; Huber and Fleck, 2001; Landis, 2002; Klinkel, 2006; Linnemann et al., 2009; Kalina et al., 2017),[2] the magnetic internal variable typically represents the evolution of the local *remanent magnetization*, which is the magnetization that remains even after the applied field is removed. Rigorous full-field numerical homogenization computations considering three-dimensional, polydisperse particle-filled representative volume elements (RVEs) of the *isotropic, nearly incompressible* h-MREs suggest that the current remanent magnetization remains independent of the mechanical stretch, but only rotates with the mechanical rotation (Mukherjee et al., 2021) (see also recent experimental evidence by Yan et al. (2021a)). Thus, we define the current internal variable to be

$$\widehat{\boldsymbol{\xi}} = \mathbf{R}\boldsymbol{\xi}, \tag{2.19}$$

where $\mathbf{R}$ is the rotation tensor obtained from the polar decomposition of $\mathbf{F} = \mathbf{R}\mathbf{U}$. Thus, the Lagrangian counterpart $\boldsymbol{\xi}$ of the current internal variable $\widehat{\boldsymbol{\xi}}$ is naturally defined in a *stretch-free intermediate configuration* $\mathcal{V}_i$ instead of the reference configuration $\mathcal{V}_0$ (see Fig. 1b). Finally, with this observation, we note that with $\boldsymbol{\xi}$ defined in $\mathcal{V}_i$, the standard materials relations (2.8) and (2.16) are also defined in $\mathcal{V}_i$.

Remark 1. The recent work of Mukherjee et al. (2021) denotes the internal variable $\boldsymbol{\xi}$ as $\boldsymbol{\mathcal{H}}^r$, whose Eulerian counterpart is denoted via $\mathbf{h}^r$. Furthermore, to express the switching surface hysteresis model in the lights of the well known small strain mechanical plasticity framework, the "total" $\mathbf{H}$ and $\mathbf{h}$ are considered to be additively decomposed into an "energetic" and a "remanent" part, so that, $\mathbf{H} = \mathbf{H}^e + \mathbf{U}\boldsymbol{\mathcal{H}}^r$ and equivalently in the current configuration $\mathbf{h} = \mathbf{h}^e + \mathbf{h}^r$. Notice that $\boldsymbol{\mathcal{H}}^r$ like $\boldsymbol{\xi}$ and $\mathbf{h}^r$ like $\widehat{\boldsymbol{\xi}}$ are defined in the intermediate and current configurations, respectively. Nonetheless, such an additive decomposition and expression of the free energy density in terms of $\mathbf{H}^e$ and $\boldsymbol{\mathcal{H}}^r$ (or equivalently, $\mathbf{h}^e$ and $\mathbf{h}^r$) is a constitutive choice, which is not adopted in the present paper. Rather, here we directly define $\boldsymbol{\xi}$ to be a remanent magnetization-like internal variable and propose the free energy densities in terms of the primary $\mathbf{H}$ (or $\mathbf{B}$) and $\boldsymbol{\xi}$.

2.4. Expressions for the total Cauchy stress

Although the constitutive model definitions are complete so far, the expression for the total Cauchy stress in terms of the current magnetic and mechanical variables are often sought after to gain more insight to the different stress contributions. Thus, the expressions for $\boldsymbol{\sigma}$ in terms of $\mathbb{B}$, $\mathbf{h}$, $\mathbf{b}$ and $\widehat{\boldsymbol{\xi}}$, where $\mathbb{B} = \mathbf{F}\mathbf{F}^T$ is the left Cauchy–Green tensor, in the $\mathbf{F}-\mathbf{H}$ and $\mathbf{F}-\mathbf{B}$ settings are provided in the following.

Cauchy stress in the $\mathbf{F}-\mathbf{H}$ *model*: We first express W^{H} in terms of $\mathbf{F}$, $\mathbf{H}$ and $\boldsymbol{\xi}$ and subsequently express it to be $W^{\mathrm{H}}(\mathbf{F},\mathbf{H},\boldsymbol{\xi}) \equiv \mathrm{w}^{\mathrm{h}}(\mathbb{B},\mathbf{h},\widehat{\boldsymbol{\xi}}) = \rho_o\psi^{\mathrm{h}}(\mathbb{B},\mathbf{h},\widehat{\boldsymbol{\xi}}) - (\mu_0/2)J\mathbf{h}\cdot\mathbf{h}$, where ψ^{h} is the Helmholtz free energy density associated with the h-MRE. Moreover, we treat the Eulerian fields to be functions of $\mathbf{F}$ (or $\mathbf{R}$) and their referential (or intermediate) counterparts, such that $\mathbf{h} = \mathbf{h}(\mathbf{F},\mathbf{H})$ and $\widehat{\boldsymbol{\xi}} = \widehat{\boldsymbol{\xi}}(\mathbf{R},\boldsymbol{\xi})$. With these, a straightforward algebraic exercise starting from the variational statement (2.3) and utilizing (2.17), (2.19) leads to (see Appendix A of Mukherjee et al. (2021) for details)

$$\boldsymbol{\sigma} = \underbrace{\frac{2\rho_0}{J}\left[\frac{\partial\psi^{\mathrm{h}}}{\partial\mathbb{B}}\right]_{\mathbf{h},\widehat{\boldsymbol{\xi}}}\mathbb{B}}_{\boldsymbol{\sigma}^{\mathrm{e}}} + \underbrace{\frac{2}{J\det\mathbf{Z}}\left[\mathbf{Z}\,\mathrm{skw}\big(\widehat{\boldsymbol{\xi}}\otimes\widehat{\boldsymbol{\eta}}\big)\mathbf{V}\mathbf{Z}\right]}_{\boldsymbol{\sigma}^{\mathrm{r}}} + \underbrace{\left[\mathbf{h}\otimes\mathbf{b} - \frac{\mu_0}{2}|\mathbf{h}|^2\mathbf{I}\right]}_{\boldsymbol{\sigma}^{\mathrm{maxw}}}, \tag{2.20}$$

where three distinct components of the total $\boldsymbol{\sigma}$, namely the elastic $\boldsymbol{\sigma}^{\mathrm{e}}$, remanent $\boldsymbol{\sigma}^{\mathrm{r}}$ and Maxwell $\boldsymbol{\sigma}^{\mathrm{maxw}}$ stress parts are obtained. In this last expression, we introduce the Eulerian counterpart of $\boldsymbol{\eta}$ to be $\widehat{\boldsymbol{\eta}} = -\rho_0[\partial\psi^{\mathrm{h}}/\partial\widehat{\boldsymbol{\xi}}]_{\mathbb{B},\mathbf{h}}$, such that, $\widehat{\boldsymbol{\eta}} = \mathbf{R}\boldsymbol{\eta}$. Moreover, in (2.20) we use the explicit fourth order tensor expression for $\partial\mathbf{R}/\partial\mathbf{F}$ from Chen and Wheeler (1993), which, in turn, introduces the tensors $\mathbf{V}$ and $\mathbf{Z}$ defined as

$$\mathbf{V} = \mathbf{F}\mathbf{R}^T \qquad \text{and} \qquad \mathbf{Z} = \mathrm{tr}[\mathbf{V}]\mathbf{I} - \mathbf{V}. \tag{2.21}$$

By its very definition from $(2.17)_1$, where $\mathbf{S}$ is given by $(2.6)_2$, the total $\boldsymbol{\sigma}$ is symmetric. However, its components $\boldsymbol{\sigma}^{\mathrm{e}}$, $\boldsymbol{\sigma}^{\mathrm{r}}$ and $\boldsymbol{\sigma}^{\mathrm{maxw}}$ are not, in general, symmetric.

Cauchy stress in the $\mathbf{F}-\mathbf{B}$ *model*: Similarly, the expression for total $\boldsymbol{\sigma}$ in the $\mathbf{F}-\mathbf{B}$ model can be obtained by first expressing $W^{\mathrm{B}}(\mathbf{F},\mathbf{B},\boldsymbol{\xi}) \equiv \mathrm{w}^{\mathrm{b}}(\mathbb{B},\mathbf{b},\widehat{\boldsymbol{\xi}}) = \psi^{\mathrm{b}}(\mathbb{B},\mathbf{b},\widehat{\boldsymbol{\xi}}) - (1/2\mu_0)J\mathbf{b}\cdot\mathbf{b}$ with the Helmholtz free energy density now expressed in terms of $\mathbb{B}$, $\mathbf{b} = \mathbf{b}(\mathbf{F},\mathbf{B})$ and $\widehat{\boldsymbol{\xi}} = \widehat{\boldsymbol{\xi}}(\mathbf{R},\boldsymbol{\xi})$. The expression for $\boldsymbol{\sigma}$ from the variational statement (2.12) and (2.17), (2.19) becomes

$$\boldsymbol{\sigma} = \underbrace{\frac{2\rho_0}{J}\left[\frac{\partial\psi^{\mathrm{b}}}{\partial\mathbb{B}}\right]_{\mathbf{b},\widehat{\boldsymbol{\xi}}}\mathbb{B}}_{\boldsymbol{\sigma}^{\mathrm{e}}} + \underbrace{\frac{2}{J\det\mathbf{Z}}\left[\mathbf{Z}\,\mathrm{skw}\big(\widehat{\boldsymbol{\xi}}\otimes\widehat{\boldsymbol{\eta}}\big)\mathbf{V}\mathbf{Z}\right]}_{\boldsymbol{\sigma}^{\mathrm{r}}} + \underbrace{\left[\mathbf{h}\otimes\mathbf{b} - \frac{\mu_0}{2}\Big(|\mathbf{h}|^2 - |\mathbf{m}|^2\Big)\mathbf{I}\right]}_{\boldsymbol{\sigma}^{\mathrm{maxw}}}, \tag{2.22}$$

where $\widehat{\boldsymbol{\eta}}$ is defined as $\widehat{\boldsymbol{\eta}} = -\rho_0[\partial\psi^{\mathrm{b}}/\partial\widehat{\boldsymbol{\xi}}]_{\mathbb{B},\mathbf{b}}$. Thus, the expressions for the elastic and remanent Cauchy stresses remain the same in the $\mathbf{F}-\mathbf{H}$ and $\mathbf{F}-\mathbf{B}$ models, of course, the latter has a free energy density ψ^{b}, while the former has ψ^{h} in their constitutive relations. Moreover, the hydrostatic part of the Maxwell stress gets modified in the case of the $\mathbf{F}-\mathbf{B}$ model, which is in agreement with the existing s-MRE constitutive models (Kankanala and Triantafyllidis, 2004; Dorfmann and Ogden, 2004; Danas, 2017).

Next, with a relative abuse in the notations,[3] we express the non-Maxwell part of $\boldsymbol{\sigma}$ to be simply the mechanical Cauchy stress contribution, so that $\boldsymbol{\sigma}^{\mathrm{mech}} = \boldsymbol{\sigma}^{\mathrm{e}} + \boldsymbol{\sigma}^{\mathrm{r}}$. Of course, not only the mechanical strains, but also the magnetic remanent fields in the h-MRE contribute to $\boldsymbol{\sigma}^{\mathrm{mech}}$. In fact, the expressions of $\boldsymbol{\sigma}^{\mathrm{r}}$ in (2.20) and (2.22) show that the remanent stress arises whenever the current remanent magnetization $\widehat{\boldsymbol{\xi}}$ and its dual $\widehat{\boldsymbol{\eta}}$ cease to be parallel. This particular scenario arises during the non-aligned loading of the h-MREs, leading to a "magnetic torque"-like contribution to the total $\boldsymbol{\sigma}$.

The Maxwell stress $\boldsymbol{\sigma}^{\mathrm{maxw}}$, on the other hand, remains independent of the material properties, while only depending on the local $\mathbf{h}$ and

[2] The works of Bassiouny et al. (1988), Huber et al. (1999), Huber and Fleck (2001), Landis (2002), Klinkel (2006) address the hysteretic polarization response of ferroelectric ceramics in a small strain setting. Nonetheless, the thermodynamic framework provided therein is identical to that for the ferromagnetic hysteresis.

[3] Perhaps the best word for this term would have been the stress in the material, i.e., $\boldsymbol{\sigma}^{\mathrm{mat}}$ to distinguish it from the Maxwell part that is present even when there is no material. Nevertheless, for historical reasons we keep here the earlier notations.

b fields at any point in the continuum. The mechanical and Maxwell parts of the first Piola–Kirchhoff stress can then be obtained directly via $\mathbf{S}^{\text{mech}} = J\boldsymbol{\sigma}^{\text{mech}}\mathbf{F}^{-T}$ and $\mathbf{S}^{\text{maxw}} = J\boldsymbol{\sigma}^{\text{maxw}}\mathbf{F}^{-T}$, such that $\mathbf{S} = \mathbf{S}^{\text{mech}} + \mathbf{S}^{\text{maxw}}$.

3. Definitions of the energy densities and dissipation potential

This section puts forth the specific energy densities and the dissipation potential for the *h*-MREs and shows the limiting cases that yield the corresponding *s*-MRE models. First, we recall for completeness the specific energy functions and the evolution law for $\boldsymbol{\xi}$ in the $\mathbf{F}-\mathbf{H}$ setting following Mukherjee et al. (2021). This will be followed by the derivation of the equivalent energy density function in terms of $\mathbf{F}-\mathbf{B}$.

In particular, here we propose a *microstructurally-guided* macroscopic continuum model for isotropic, incompressible *h*-MREs in terms of several material parameters attributed to the pure elastomeric matrix or the hard magnetic particle phase and the particle volume fraction. Moreover, the central idea of the microstructurally-guided modeling remains of its ability to yield a number of analytical homogenization estimates under different limits of the purely mechanical and magnetic responses.

3.1. $\mathbf{F}-\mathbf{H}$ *model*

We now provide the specific forms of $W^{\text{H}}(\mathbb{C},\mathbf{H},\boldsymbol{\xi})$ and $D(\dot{\boldsymbol{\xi}})$[4] in terms of several invariants, which satisfy the material frame indifference and material symmetry conditions for the isotropic *h*-MREs. These invariants include *purely mechanical* invariants, namely

$$I_1 = \text{tr}\mathbb{C}, \qquad I_2 = \frac{1}{2}\left[(\text{tr}\mathbb{C})^2 - \text{tr}\mathbb{C}^2\right], \qquad J = \sqrt{\det\mathbb{C}}, \tag{3.1}$$

which are standard in the isotropic hyperelastic material models. Moreover, a set of magneto-mechanical invariants based on $\mathbf{H}$, $\boldsymbol{\xi}$ and $\mathbb{C}$ is defined to be

$$I_4^{\text{HH}} = \mathbf{H}\cdot\mathbf{H}, \qquad I_4^{\text{H}\xi} = \mathbf{H}\cdot\mathbb{C}^{1/2}\boldsymbol{\xi}, \qquad I_4^{\xi\xi} = \boldsymbol{\xi}\cdot\mathbb{C}\boldsymbol{\xi} \tag{3.2}$$

$$I_5^{\text{HH}} = \mathbf{H}\cdot\mathbb{C}^{-1}\mathbf{H}, \qquad I_5^{\text{H}\xi} = \mathbf{H}\cdot\mathbb{C}^{-1/2}\boldsymbol{\xi}, \qquad I_5^{\xi\xi} = \boldsymbol{\xi}\cdot\boldsymbol{\xi}. \tag{3.3}$$

While the invariants I_i^{HH} $(i = 4,5)$ are standard in the finite strain modeling of the *s*-MREs (Javili et al., 2013; Lefère and Lopez-Pamies, 2017; Mukherjee et al., 2020), the remaining invariants in (3.2) and (3.3) are the additional invariants introduced in the *h*-MRE model. All these invariants satisfy the material frame indifference and the material symmetry conditions. Notably, the I_5-based invariants are also referred to be the "purely magnetic" invariants (Danas, 2017; Mukherjee et al., 2020, 2021; Polukhov and Keip, 2021). This is because the I_5 invariants are expressed only in terms of the current magnetic fields and internal variable (those written on the current configuration in Fig. 1b), which, in turn, leads to no intrinsic magneto-mechanical material coupling in the MRE local response under a uniformly applied Eulerian magnetic field. This, however, does not imply that a solid described only in terms of I_5 invariants does not exhibit structural coupling, where resulting magnetic fields may be highly non-uniform (see for instance Psarra et al. (2019) and Dorn et al. (2021)).

We now express the energy density associated with the *h*-MRE in terms of these invariants. In particular, W^{H} is considered to be the sum of three distinct energy densities, namely, the pure mechanical, pure magnetic and coupling free energy density, such that

$$W^{\text{H}}(I_1,J,I_4^{\text{H}\xi},I_4^{\xi\xi},I_5^{\text{HH}},I_5^{\text{H}\xi},I_5^{\xi\xi}) = \begin{cases} \rho_0\Psi_{\text{mech}}(I_1) + \rho_0\Psi^{\text{H}}_{\text{mag}}(I_5^{\text{HH}},I_5^{\text{H}\xi},I_5^{\xi\xi}) \\ \quad +\rho_0\Psi^{\text{H}}_{\text{couple}}(I_4^{\text{H}\xi},I_4^{\xi\xi},I_5^{\text{H}\xi},I_5^{\xi\xi}) - \dfrac{\mu_0}{2}I_5^{\text{HH}} & \text{if } J=1 \\ +\infty & \text{otherwise,} \end{cases} \tag{3.4}$$

where ρ_0 is the reference density of the solid. The last term $\mu_0 I_5^{\text{HH}}/2$ in (3.4) represents the energy associated with free space with μ_0 being the magnetic permeability of vacuum. Thus, even in absence of any material, the energy density in the magneto-mechanical formulation does not vanish.

The purely mechanical free energy density $\rho_0\Psi_{\text{mech}}$ for the *h*-MRE is considered to be the analytical homogenization estimate by Lopez-Pamies et al. (2013) for the two-phase particle-matrix, incompressible composites, so that

$$\Psi_{\text{mech}}(I_1) = (1-c)\Psi_{\text{m,mech}}(\mathcal{I}_1), \qquad \mathcal{I}_1 = \frac{I_1-3}{(1-c)^{7/2}} + 3, \tag{3.5}$$

where c is the particle volume fraction and $\Psi_{\text{m,mech}}$ is the free energy density of the matrix. Notably, the homogenization estimate (3.5) holds for any I_1-based incompressible particle-matrix composite. Thus, the choice for the matrix constitutive law remains open in the preset modeling framework. Evidently, $\Psi_{\text{mech}}(I_1)$ becomes $\Psi_{\text{m,mech}}(I_1)$, i.e., the matrix free energy for $c=0$, whereas, $\Psi_{\text{mech}}(I_1)$ tends to $+\infty$ in the limit of $c\to 1$, hence, modeling a rigid material.

The introduction of such an incompressible material model necessitates the modification of the constitutive relations $(2.6)_2$ and $(2.14)_2$ for the total stress $\mathbf{S}$ to be

$$\mathbf{S} = 2\mathbf{F}\frac{\partial W^{\text{H}}}{\partial\mathbb{C}} + p\mathbf{F}^{-T}, \qquad \text{and} \qquad \mathbf{S} = 2\mathbf{F}\frac{\partial W^{\text{B}}}{\partial\mathbb{C}} + p\mathbf{F}^{-T}, \tag{3.6}$$

respectively, where p is the Lagrange multiplier associated with the incompressibility constraint $J=1$. In practice, p adds on to the local (point wise) number of unknowns to be solved for from the variational principle. Further discussion on the practical aspects of dealing with incompressibility is provided under Remark 3.

Next, the magnetic and coupling free energy functions along with the dissipation potential are proposed. Special care is taken in proposing these functions so that the magnetization response yields several limiting cases, especially, in the limit of small primary and remanent magnetic fields. In the following we provide these functions without elaborating on their individual significance. In turn, the main features of the switching surface hysteresis model and its limiting case yielding the saturation-type non-hysteretic soft magnetic response will be discussed in Section 3.2.

The pure magnetic free energy is expressed in terms of the I_5-based invariants, so that

$$\rho_0\Psi^{\text{H}}_{\text{mag}}(I_5^{\text{HH}},I_5^{\text{H}\xi},I_5^{\xi\xi}) = -\frac{\mu_0}{2}\chi^e I_5^{\text{HH}} + \mu_0(1+\chi^e)I_5^{\text{H}\xi} + \frac{\mu_0}{2}\left(\frac{1-c}{3c}\right)I_5^{\xi\xi} + \frac{\mu_0}{c}\frac{(m^s)^2}{\chi^r_{\text{p}}}f_{\text{p}}\left(\frac{\sqrt{I_5^{\xi\xi}}}{m^s}\right), \tag{3.7}$$

where χ^r_{p} is the *remanent susceptibility* of the underlying magnetic particle, whereas the "effective" parameters χ^e and m^s for the composite are given in terms of the particle magnetic properties and its volume fraction c as

$$\chi^e = \frac{3c\chi^e_{\text{p}}}{3+(1-c)\chi^e_{\text{p}}}, \qquad m^s = c\, m^s_{\text{p}}\left(\frac{1+\chi^e_{\text{p}}}{1+\chi^e}\right), \tag{3.8}$$

where χ^e_{p} and m^s_{p} are the particle *energetic susceptibility* and *saturation magnetization* (a graphic explanation of these parameters is provided later in the context of Fig. 2). Moreover, $f_{\text{p}}(x)$ is a nonlinear function

[4] For clarity, we note here that in the earlier work of Mukherjee et al. (2021), the symbol $\mathcal{H}^r \equiv \boldsymbol{\xi}$ has been used to denote the internal variable. Nevertheless, in the present work, we use the same $\boldsymbol{\xi}$ variable for both $\mathbf{F}-\mathbf{H}$ and $\mathbf{F}-\mathbf{B}$ formulations and to avoid any confusion, we have prompted for a neutral symbol.

that leads to a saturation-type magnetization behavior. Additionally, $f_{\rm p}(x)$ must satisfy the properties such that (i) it is smooth and at least twice differentiable for all $0 \le x < 1$, (ii) $f_{\rm p}'(x)$ leading to an inverse saturation (sigmoid) function that tends to $+\infty$ in the limit of $x \to 1$ and (iii) the leading order Taylor series expansion of $f_{\rm p}(x)$ around $x = 0$ is $0.5x^2$. Of course, the specific choices for $f_{\rm p}(x)$ depends on the saturation response of the (hard/soft) magnetic particles. A couple of specific choices for the hard magnetic NdFeB and soft magnetic iron particles are provided in Section 4.

Finally, the coupling free energy $\Psi^{\rm H}_{\rm couple}$ is proposed in terms of both, the I_4 and I_5-based invariants as defined in (3.2) and (3.3), so that

$$\rho_0 \Psi^{\rm H}_{\rm couple}(I_4^{{\rm H}\xi}, I_4^{\xi\xi}, I_5^{{\rm H}\xi}, I_5^{\xi\xi}) = c\ \beta(c)\mu_0 \Big[\big(I_4^{\xi\xi} - I_5^{\xi\xi}\big) - 2\chi^e \big(I_4^{{\rm H}\xi} - I_5^{{\rm H}\xi}\big) \Big]. \quad (3.9)$$

Notice that the I_4-type "coupling" invariants in $W^{\rm H}$ only appear in the coupling free energy, whereas, the purely magnetic free energy (3.7) is only a function of the "pure magnetic" or "decoupled" I_5-type invariants. Moreover, the coupling parameter $\beta(c)$ in (3.9) requires to be calibrated against experimental data or numerical homogenization estimates. Specifically, we will present the calibration of $\beta(c)$ against the full-field numerical homogenization estimates in Section 4. We also note the simple linear dependence on the invariants of the coupled energy density in (3.9). This will prove extremely useful in obtaining a dual energy density for the $\mathbf{F}-\mathbf{B}$ model.

Dissipation potential: It remains to define the dissipation potential D, which along with $W^{\rm H}$ completes the local constitutive model definitions. Thus, we propose the dissipation potential to be a simple power law in terms of $\dot{\boldsymbol{\xi}}$, so that

$$D(\dot{\boldsymbol{\xi}}) = \frac{n\ b^c}{n+1} |\dot{\boldsymbol{\xi}}|^{\frac{n+1}{n}}, \qquad \text{with} \quad 1 \le n < +\infty, \quad (3.10)$$

where b^c is the effective *coercive field* of the composite that is given in terms of the particle coercivity along with the particle and effective energetic susceptibility, so that

$$b^c = b^c_{\rm p} \left(\frac{1+\chi^e}{1+\chi^e_{\rm p}} \right)^{4/5}, \quad (3.11)$$

with $b^c_{\rm p}$ being the particle coercivity. Typically, for a hard-magnetic composite the effective coercivity is given by $b^c = b^c_{\rm p}$ (Idiart et al., 2006). Nonetheless, the term multiplying $b^c_{\rm p}$ in (3.11) essentially serves as a correction term for an actual magnet, whose saturation magnetization slope is *not* identically zero.

The dissipation potential $D(\dot{\boldsymbol{\xi}})$ in (3.10) is strictly convex (except for $n = +\infty$ that becomes simply convex), hence, satisfies the dissipation inequality constraint. Moreover, the rate $|\dot{\boldsymbol{\xi}}| = \sqrt{\dot{\boldsymbol{\xi}} \cdot \dot{\boldsymbol{\xi}}}$ satisfies the material frame indifference and material symmetry conditions. By observing the experimental data on magnetic materials, we focus next on a *rate-independent* ferromagnetic hysteresis model. Thus, we consider the limiting case $n = +\infty$ at which, the dissipation potential (3.10) becomes $D(\dot{\boldsymbol{\xi}}) = b^c |\dot{\boldsymbol{\xi}}|$, whose derivative with respect to $\dot{\boldsymbol{\xi}}$ is non-unique at $|\dot{\boldsymbol{\xi}}| = 0$. Hence, we start from the Legendre–Fenchel transform of D, i.e., D^η such that

$$D^\eta(\boldsymbol{\eta}) = \inf_{\dot{\boldsymbol{\xi}}} \Big[\boldsymbol{\eta} \cdot \dot{\boldsymbol{\xi}} - b^c |\dot{\boldsymbol{\xi}}| \Big] \quad (3.12)$$

in the rate-independent limit. The minimization condition of the last expression leads to a criterion known as *ferromagnetic switching surface*

$$\Phi(\boldsymbol{\eta}) := \boldsymbol{\eta} \cdot \boldsymbol{\eta} - (b^c)^2 = 0, \quad (3.13)$$

which must be satisfied during the energy dissipation in a magnetic loading/unloading cycle. With (3.13), we rephrase the dissipation potential $D(\dot{\boldsymbol{\xi}})$ by introducing a (non-negative) Lagrange multiplier $\dot{\Lambda}$, so that

$$D(\dot{\boldsymbol{\xi}}) = \sup_{\boldsymbol{\eta}} \inf_{\dot{\Lambda} \ge 0} \Big[\boldsymbol{\eta} \cdot \dot{\boldsymbol{\xi}} - \dot{\Lambda} \Phi(\boldsymbol{\eta}) \Big]. \quad (3.14)$$

In fact, substituting $\boldsymbol{\eta} = b^c \dot{\boldsymbol{\xi}}/|\dot{\boldsymbol{\xi}}|$ (the minimization condition of (3.12)) yields exactly $D(\dot{\boldsymbol{\xi}}) = b^c |\dot{\boldsymbol{\xi}}|$ but now with a constraint (3.13), which must be satisfied to make the term $\dot{\Lambda}\Phi(\boldsymbol{\eta})$ in (3.14) to vanish.

The constrained dissipation potential in (3.14) thus needs to be employed in the variational principle (2.3) to obtain a set of equations involved in obtaining the evolution of $\boldsymbol{\xi}$. These stationarity conditions of (3.14) are

$$\dot{\boldsymbol{\xi}} = \dot{\Lambda} \frac{\partial \Phi}{\partial \boldsymbol{\eta}}, \qquad \Phi(\boldsymbol{\eta}) \le 0, \qquad \dot{\Lambda} \ge 0 \qquad \text{and} \qquad \dot{\Lambda}\Phi = 0, \quad (3.15)$$

where the latter three is commonly referred to be the Kraush–Kuhn–Tucker (KKT) conditions. With (3.15), the evolution equation for the internal variable $\boldsymbol{\xi}$ is now fully defined.

3.2. Discussion on the particle and effective hysteresis responses

The definition of the $\mathbf{F}-\mathbf{H}$ constitutive model becomes complete in terms of fully specifying the energy (3.4) and the dissipation (3.15) potentials. This section elaborates on the key properties of the hysteresis response obtained from the proposed variational principle (2.3). Note that the practical aspects of numerically solving the equations deriving from (2.3) will be detailed in Section 4.

We first show a representative particle magnetic hysteresis response obtained for $c = 1$ in Fig. 2a. Both, ideal ($\chi^e_{\rm p} = 0$) and actual ($\chi^e_{\rm p} > 0$) hysteresis loops are shown on Fig. 2a along with the initial slopes $\chi^e_{\rm p}$ and $\chi^r_{\rm p}(1+\chi^e_{\rm p})^2 + \chi^e_{\rm p}$ of, respectively, the energetic and remanent magnetization. In fact, the remanent magnetization initiates once the switching criteria $\Phi(\boldsymbol{\eta}) = 0$ is satisfied. This initiation point is termed as the "switching point", which is indicated on Fig. 2a to be $h_1 = b^c_{\rm p}/[(1+\chi^e_{\rm p})\mu_0]$. The magnetization, after a subsequent increase following the switching, gradually acquires the effective energetic magnetization slope of $\chi^e_{\rm p}$. The ideal $m-h$ hysteresis loop, on the other hand, exhibits a magnetization response that saturates at the saturation magnetization $m^s_{\rm p}$.

The evolution of the remanent internal variable $\boldsymbol{\xi}$ under the same applied $\mathbf{h} = h_1 \mathbf{e}_1$ is shown in Fig. 2b. The responses shown therein exhibit the qualitative nature of $\boldsymbol{\xi} \sim -\mathbf{m}$. In fact, for the ideal hysteresis response the magnetization reads $\mathbf{m} = -\boldsymbol{\xi}$. However, the last relation does *not* hold for the non-ideal hysteresis loops and for the coupled magneto-mechanical analysis where $\mathbb{C} \neq \mathbf{I}$. Moreover, the slope of the $\xi_1 - h_1$ response immediately after the switching is $-\chi^r_{\rm p}$ for all $\chi^e_{\rm p} \ge 0$.

Finally, the important limiting case that allows to retrieve the saturation-type reversible magnetization response from the proposed dissipative framework is shown in Fig. 2c. As pointed out by Mukherjee and Danas (2019), the switching surface framework leads to the typical saturation-type, non-hysteretic magnetization response when the coercive field $b^c_{\rm p}$ becomes vanishingly small. Specifically, the switching condition for $b^c_{\rm p} = 0$ leads to $\boldsymbol{\eta} = \mathbf{0}$, which, in turn, yields $\boldsymbol{\xi}$ to be an algebraic function of $\mathbf{H}$. Moreover, this limit-valid *mutatis-mutandis* for the h-MREs–leads to a non-hysteretic s-MRE model. Thus, the proposed h-MRE model is shown to be a general modeling framework for the MREs, whose response for $b^c_{\rm p} = 0$ and $\chi^e_{\rm p} = 0$ leads to a constitutive model for an s-MRE. In fact, substituting $\boldsymbol{\eta} = \widehat{\boldsymbol{\eta}} = \mathbf{0}$ into the expressions for $\boldsymbol{\sigma}$ in (2.20) and (2.22), we observe that the remanent stress $\check{\boldsymbol{\sigma}}^{\rm r}$ vanishes identically, recovering the $\boldsymbol{\sigma}$ expressions for the s-MREs as derived by Kankanala and Triantafyllidis (2004).

Since the magneto-mechanical coupling at the material level does *not* affect the magnetization response of the MRE as a whole (Danas, 2017; Bodelot et al., 2017; Mukherjee et al., 2020, 2021), the hysteresis response of the composite exhibits the same features as discussed for the particle hysteresis except now the initial slopes of energetic and remanent magnetization are given in terms of the "effective" susceptibility measures χ^e and χ^r. While χ^e is given by $(3.8)_1$, we obtain the effective χ^r while expressing $\Psi^{\rm H}_{\rm mag}$ in the limit of $|\boldsymbol{\xi}| \to 0$, so that (3.7)

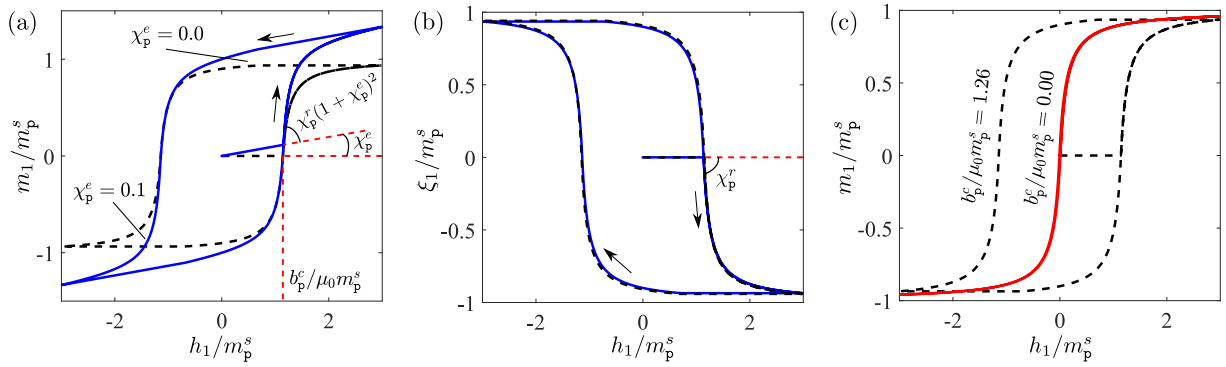

Fig. 2. (a) Magnetization response under applied uniaxial cyclic h-field $\mathbf{h}=h_1\mathbf{e}_1$. Both ideal ($\chi^e_{\rm p}=0$) and actual ($\chi^e_{\rm p}>0$) hysteresis loops are shown along with the slopes of the $m-h$ response before and after switching. (b) Evolution of the internal variable ξ under the same load for both actual and ideal hysteresis cases. (c) Magnetization responses for finite and zero coercivity leading to, respectively, hysteretic and energetic magnetization responses.

becomes

$$\rho_0\Psi^{\rm H}_{\rm mag}(I_5^{\rm HH},I_5^{{\rm H}\xi},I_5^{\xi\xi})=-\frac{\mu_0}{2}\chi^e I_5^{\rm HH}+\mu_0(1+\chi^e)I_5^{{\rm H}\xi}+\frac{\mu_0}{2\chi^r}I_5^{\xi\xi}+\mathcal{O}(|\xi|^3),$$
$$\chi^r=\frac{3c\chi^r_{\rm p}}{3+(1-c)\chi^r_{\rm p}}. \tag{3.16}$$

In fact, these definitions of χ^e and χ^r are the classical Maxwell–Garnet homogenization estimates for the effective susceptibility for the isotropic two phase composites comprising a magnetic and a non-magnetic phase (Lefère and Lopez-Pamies, 2017). Moreover, the model yields an effective saturation magnetization $m^s\approx cm^s_{\rm p}$ and coercivity $b^c\approx b^c_{\rm p}$, which are, in turn, identical to their respective analytical homogenization estimates (Lefère and Lopez-Pamies, 2017). Of course, here we introduce suitable correction terms to these analytical estimates in order to obtain more accurate model response specifically for the h-MREs having $\chi^e>0$.

3.3. $\mathbf{F}-\mathbf{B}$ *model*

The proposed $W^{\rm H}$ in (3.4) along with the invariants in (3.2) and (3.3) lead to a *strictly concave* energy density function in terms of $\mathbf{H}$, i.e., for a given $\mathbb{C}$ and ξ, $W^{\rm H}$ is a strictly concave function of $\mathbf{H}$. Consequently, in order to obtain an equivalent $\mathbf{F}-\mathbf{B}$ energy density, we seek for a closed form partial Legendre–Fenchel transform of $W^{\rm H}$ following $(2.11)_2$. Straightforward algebraic manipulations lead to the expression for $W^{\rm B}(\mathbb{C},\mathbf{B},\xi)$ such that

$$W^{\rm B}(I_1,J,I_4^{\xi\xi},I_5^{\rm BB},I_5^{{\rm B}\xi},I_5^{\xi\xi},I_6^{{\rm B}\xi},I_6^{\xi\xi})=\begin{cases}\rho_0\Psi_{\rm mech}(I_1)+\rho_0\Psi^{\rm B}_{\rm mag}(I_5^{\rm BB},I_5^{{\rm B}\xi},I_5^{\xi\xi})\\ \quad+\rho_0\Psi^{\rm B}_{\rm couple}(I_4^{\xi\xi},I_5^{{\rm B}\xi},I_5^{\xi\xi},I_6^{{\rm B}\xi},I_6^{\xi\xi})+\dfrac{1}{2\mu_0}I_5^{\rm BB} & \text{if } J=1\\ +\infty & \text{otherwise.}\end{cases} \tag{3.17}$$

The new $\mathbf{B}$ and ξ-based invariants introduced in the last expression are defined as

$$I_5^{\rm BB}=\mathbf{B}\cdot\mathbb{C}\mathbf{B},\qquad I_5^{{\rm B}\xi}=\mathbf{B}\cdot\mathbb{C}^{1/2}\xi,\qquad I_6^{{\rm B}\xi}=\mathbf{B}\cdot\mathbb{C}^{3/2}\xi\quad\text{and}$$
$$I_6^{\xi\xi}=\xi\cdot\mathbb{C}^2\xi. \tag{3.18}$$

Notice that the above invariants appear naturally in the course of obtaining the Legendre–Fenchel transform. The first among these invariants is the standard I_5 invariant based on $\mathbf{B}$ and $\mathbb{C}$ that is employed widely in the $\mathbf{F}-\mathbf{B}$-based s-MRE modeling (Kankanala and Triantafyllidis, 2004; Ponte Castañda and Galipeau, 2011; Danas et al., 2012; Danas, 2017; Mukherjee et al., 2020). The other invariants in (3.18) are the mixed or purely remanent ones, which appear only in the modeling of h-MREs. Moreover, the mixed invariants when expressed in terms of the current quantities ($\mathbf{b}$, $\widehat{\boldsymbol{\xi}}$) reads $I_5^{{\rm B}\xi}=\mathbf{b}\cdot\widehat{\boldsymbol{\xi}}$ and $I_6^{{\rm B}\xi}=\mathbf{b}\cdot\mathbb{B}\widehat{\boldsymbol{\xi}}$, thus, asserting the fact that I_5-based invariants yield no magneto-mechanical coupling under applied Eulerian magnetic field.

The mechanical free energy $\Psi_{\rm mech}$ in (3.17) remains identical to (3.5), whereas the transformed magnetic free energy $\Psi^{\rm B}_{\rm mag}(I_5^{\rm BB},I_5^{{\rm B}\xi},I_5^{\xi\xi})$ becomes

$$\rho_0\Psi^{\rm B}_{\rm mag}(I_5^{\rm BB},I_5^{{\rm B}\xi},I_5^{\xi\xi})=-\frac{1}{2\mu_0}\frac{\chi^e}{1+\chi^e}I_5^{\rm BB}+I_5^{{\rm B}\xi}+\frac{\mu_0}{2}\left(\chi^e+\frac{1+2c}{3c}\right)I_5^{\xi\xi}$$
$$+\frac{\mu_0}{c}\frac{(m^s)^2}{\chi^r_{\rm p}}f_{\rm p}\left(\frac{\sqrt{I_5^{\xi\xi}}}{m^s}\right), \tag{3.19}$$

where all the model parameters along with the function $f_{\rm p}(x)$ remain identical to their respective definitions in Section 3.1. Finally, the coupling free energy reads

$$\rho_0\Psi^{\rm B}_{\rm couple}(I_4^{\xi\xi},I_5^{{\rm B}\xi},I_5^{\xi\xi},I_6^{{\rm B}\xi},I_6^{\xi\xi})=c\beta\left[\mu_0(1-2\chi^e)\left\{I_4^{\xi\xi}-I_5^{\xi\xi}\right\}-\frac{2\chi^e}{1+\chi^e}\left\{I_6^{{\rm B}\xi}-I_5^{{\rm B}\xi}\right\}\right]$$
$$+2\mu_0\frac{(c\beta\chi^e)^2}{1+\chi^e}\left\{I_5^{\xi\xi}+I_6^{\xi\xi}-2I_4^{\xi\xi}\right\}. \tag{3.20}$$

Notice further that the particle volume fraction remains limited to $c\le 0.3$ in all the practical applications of h-MREs (Zhao et al., 2019; Alapan et al., 2020). Consequently, we obtain $0<\chi^e\ll 1$ for the h-MREs comprising NdFeB particles. Thus, the last term in the expression for $\rho_0\Psi^{\rm B}_{\rm couple}$ in (3.20) turns out to be substantially smaller than the preceding ones and hence, can be dropped for all practical modeling purposes. Consequently, the coupling energy in the proposed $\mathbf{F}-\mathbf{B}$ model simplifies to

$$\rho_0\Psi^{\rm B}_{\rm couple}(I_4^{\xi\xi},I_5^{{\rm B}\xi},I_5^{\xi\xi},I_6^{{\rm B}\xi},I_6^{\xi\xi})$$
$$=c\beta(c)\left[\mu_0(1-2\chi^e)\left\{I_4^{\xi\xi}-I_5^{\xi\xi}\right\}-\frac{2\chi^e}{1+\chi^e}\left\{I_6^{{\rm B}\xi}-I_5^{{\rm B}\xi}\right\}\right]. \tag{3.21}$$

With this, the definition of the $\mathbf{F}-\mathbf{B}$ based energy density becomes complete. Notice that the dissipation potential defined via (3.10) is independent of $\mathbf{H}$ and thus, remains the same for the $\mathbf{F}-\mathbf{B}$ model. Hence, here also, the switching surface and the evolution equation for ξ are defined via (3.13) and (3.15), respectively.

Being the closed-form Legendre–Fenchel transform of the $\mathbf{F}-\mathbf{H}$ model, the derived $\mathbf{F}-\mathbf{B}$ model exhibits the *exact* same features discussed in Section 3.2. Consequently, no further calibration of $\beta(c)$ parameter is needed in (3.21). Specific comparisons between the local responses of the $\mathbf{F}-\mathbf{H}$ and $\mathbf{F}-\mathbf{B}$ models will be shown next following three remarks.

Remark 2. A similar exercise of proposing equivalent, explicit models *exclusively* for the s-MREs has been carried out by Mukherjee et al.

(2020). Being non-dissipative in nature, those s-MRE models were proposed entirely in terms of $\mathbf{F}-\mathbf{H}$ or $\mathbf{F}-\mathbf{B}$ invariants. Consequently, the pure magnetic and coupling energy functions need to become notoriously nonlinear in terms of $\mathbf{H}$ (or $\mathbf{B}$) in order to capture the magnetic saturation and magnetostriction responses. Thus, a closed form Legendre–Fenchel transformation of the $\mathbf{F}-\mathbf{H}$-based energy density in terms of $\mathbf{F}-\mathbf{B}$ or *vice-versa* was not possible in that study. In contrast, in the present work of a "more general" h-MRE model, the nonlinear saturation-type magnetization and magnetostriction responses are modeled in terms of the internal variable $\boldsymbol{\xi}$, while the "energetic" magnetization and magnetostriction before switching remain linear in $\mathbf{H}$ (or $\mathbf{B}$). This key feature of the h-MRE models makes the energy density W^{H} (or W^{B}) strictly concave (or convex) in terms of the primary $\mathbf{H}$ (or $\mathbf{B}$), thus, admitting a closed form Legendre–Fenchel transform. Hence, the equivalent $\mathbf{F}-\mathbf{H}$ and $\mathbf{F}-\mathbf{B}$-based energy densities are obtained in closed forms for the more general case of h-MREs as well as for the limiting case of s-MREs.

Remark 3. The limiting case of $c=0$ leads to the energy densities associated with the non-magnetic elastomer for both, $\mathbf{F}-\mathbf{H}$ and $\mathbf{F}-\mathbf{B}$ models. Specifically, the condition $c=0$ leads to the magnetic free energies (for both the models) so that

$$\rho_0\Psi^{\mathrm{H/B}}_{\mathrm{mag}}=\begin{cases}+\infty & \text{if} \quad \boldsymbol{\xi}\neq\mathbf{0},\\ 0 & \text{if} \quad \boldsymbol{\xi}=\mathbf{0}.\end{cases} \tag{3.22}$$

This condition essentially constraints $\boldsymbol{\xi}$ to remain $\mathbf{0}$ for $c=0$. Thus, the dissipation potential (3.10) vanishes and the energy densities for the $\mathbf{F}-\mathbf{H}$ and $\mathbf{F}-\mathbf{B}$ models read, respectively, $W^{\mathrm{H}}_{c=0}=\rho_0\Psi_{\mathrm{mech}}(I_1)-(\mu_0/2)I_5^{\mathrm{HH}}$ and $W^{\mathrm{B}}_{c=0}=\rho_0\Psi_{\mathrm{mech}}(I_1)+(1/2\mu_0)I_5^{\mathrm{BB}}$. The limit of $c\to 1$, on the other hand, leads to the mechanically rigid hard-magnetic particle response, essentially yielding the pure magnetic switching surface model.

Remark 4. We note that the *quasi incompressible* equivalents of the proposed incompressible models are often useful in the numerical computations. Thus, we extend the proposed $\mathbf{F}-\mathbf{H}$ and $\mathbf{F}-\mathbf{B}$-based MRE models in a rather ad-hoc way so that the energy densities read

$$\begin{aligned}W^{\mathrm{H}}_{\mathrm{comp}}(I_1,J,I_4^{\mathrm{H}\xi},I_4^{\xi\xi},I_5^{\mathrm{HH}},I_5^{\mathrm{H}\xi},I_5^{\xi\xi})&=\rho_0\Psi^{\mathrm{comp}}_{\mathrm{mech}}(I_1,J)+\rho_0\Psi^{\mathrm{H}}_{\mathrm{mag}}(I_5^{\mathrm{HH}},I_5^{\mathrm{H}\xi},I_5^{\xi\xi})\\&+\rho_0\Psi^{\mathrm{H}}_{\mathrm{couple}}(I_4^{\mathrm{H}\xi},I_4^{\xi\xi},I_5^{\mathrm{H}\xi},I_5^{\xi\xi})-\frac{\mu_0}{2}JI_5^{\mathrm{HH}}\end{aligned} \tag{3.23}$$

and

$$\begin{aligned}W^{\mathrm{B}}_{\mathrm{comp}}(I_1,J,I_4^{\xi\xi},I_5^{\mathrm{BB}},I_5^{\mathrm{B}\xi},I_5^{\xi\xi},I_6^{\mathrm{B}\xi})&=\rho_0\Psi^{\mathrm{comp}}_{\mathrm{mech}}(I_1,J)+\rho_0\Psi^{\mathrm{B}}_{\mathrm{mag}}(I_5^{\mathrm{BB}},I_5^{\mathrm{B}\xi},I_5^{\xi\xi})\\&+\rho_0\Psi^{\mathrm{B}}_{\mathrm{couple}}(I_4^{\xi\xi},I_5^{\mathrm{B}\xi},I_5^{\xi\xi},I_6^{\mathrm{B}\xi})+\frac{I_5^{\mathrm{BB}}}{2\mu_0 J},\end{aligned} \tag{3.24}$$

respectively. The term $\Psi^{\mathrm{comp}}_{\mathrm{mech}}(I_1,J)$ in (3.23) and (3.24), given by

$$\begin{aligned}&\rho_0\Psi^{\mathrm{comp}}_{\mathrm{mech}}(I_1,J)=(1-c)\rho_0\Psi_{\mathrm{m,mech}}(I_1^{\mathrm{comp}})+\frac{G_{\mathrm{m}}'}{2(1-c)^6}(J-1)^2,\\&I_1^{\mathrm{comp}}=\frac{I_1-3-2\ln J}{(1-c)^{7/2}}+3,\end{aligned} \tag{3.25}$$

is the *nearly incompressible* approximation of the analytical effective mechanical free energy density (3.5). We typically set the Lamé parameter $G_{\mathrm{m}}'>500G_{\mathrm{m}}$, which ensures a nearly incompressible response delivering $J\approx 1$.

4. Local magneto-mechanical response

The local (point wise) model response is now computed for both, $\mathbf{F}-\mathbf{H}$ and $\mathbf{F}-\mathbf{B}$ models and compared to the numerically computed effective response for the h- and s-MREs. The numerical homogenization computations for the effective response are carried out via considering three-dimensional RVEs having spherical particle inclusions, which are either hard or soft magnets. The local energy densities for the elastomer and particle phases in the RVE are obtained directly by substituting $c=0$ and $c=1$ in the proposed model, respectively (see the discussion under Remark 3 for the energy density functions with $c=0$). In particular, we use the scalar potential-based $\mathbf{F}-\mathbf{H}$ model in the RVE computations to reduce the computational cost. The reader is referred to (Mukherjee et al., 2020, 2021) for the details on the numerical homogenization computations and its artifacts.

The following provides specific choices for the matrix hyperelastic model, the magnetic particle hardening function f_{p} and the magnetic material parameters, which are then employed in comparing the macroscopic model and microscopic RVE computed results. Note that the following choices remain the same for both, $\mathbf{F}-\mathbf{H}$ and $\mathbf{F}-\mathbf{B}$ models.

4.1. Choice of matrix hyperelastic model

The hyperelastic matrix is considered to be a simple I_1-based, incompressible Neo-hookean material, so that the free energy density associated with it reads

$$\Psi_{\mathrm{mech,m}}(I_1)=\frac{G_{\mathrm{m}}}{2}(I_1-3), \tag{4.1}$$

where G_{m} is the shear modulus of the matrix. Of course, the numerical RVE computations considers a *nearly incompressible* equivalent of (4.1) given by

$$\Psi^{\mathrm{compr}}_{\mathrm{mech,m}}(I_1,J)=\frac{G_{\mathrm{m}}}{2}(I_1-3-2\ln J)+\frac{G_{\mathrm{m}}'}{2}(J-1)^2. \tag{4.2}$$

In fact, one can derive the last equation directly by substituting $c=0$ in (3.25). We set $G_{\mathrm{m}}'=500G_{\mathrm{m}}$ to obtain all the FE computed results to follow.

4.2. Choice of magnetic particle models

We choose the hard and soft magnetic parameters along with the non-linear hardening functions f_{p} for the respective cases. While the rare earth-based NdFeB particles (commercially known as MQP particles) are the most used filler in the h-MREs (Kim et al., 2018; Zhao et al., 2019; Ren et al., 2019; Alapan et al., 2020), the s-MREs typically contain the carbonyl iron particles (CIPs) as a filler (Danas et al., 2012; Bodelot et al., 2017; Psarra et al., 2017; Dorn et al., 2021).

We first fit the model hysteresis response to the experimental NdFeB hysteresis data to obtain the model parameters. Specifically, Mukherjee and Danas (2019) show that the function

$$f_{\mathrm{p}}(x)=f_{\mathrm{hard}}(x)=-\Big[x+\ln(1-x)\Big], \qquad 0\le x<1 \tag{4.3}$$

in (3.7) (or (3.19)) describes best the saturation response of the NdFeB particles.

The soft CIPs, on the other hand, exhibit a Langevin-type saturation (Psarra et al., 2017; Bodelot et al., 2017; Danas, 2017), which is a stiffer saturation function compared to $x/(1+x)$ that is obtained from (4.3) (Mukherjee and Danas, 2019). Thus, a different $f_{\mathrm{p}}(x)$ must be employed for the s-MREs, so that $f_{\mathrm{p}}'(x)=\mathcal{L}^{-1}(x)$, where $\mathcal{L}^{-1}(x)$ is the inverse Langevin function. Unfortunately, $\mathcal{L}^{-1}(x)$ has no unique algebraic expression. Nevertheless, we use the expression[5]

$$\begin{aligned}f_{\mathrm{p}}(x)=f_{\mathrm{soft}}(x)=-\frac{1}{3}\Big[&x-x^2+\frac{x^3}{3}+\ln(1-x)+\cos(3.5x)\big\{0.0571x^2-0.0093\big\}\\&-0.0327x\sin(3.5x)+0.0093\Big],\end{aligned} \tag{4.4}$$

which is smooth differentiable for all $0\le x<1$ (see Fig. 3a). For comparison we plot the $f_{\mathrm{p}}(x)$ and $f_{\mathrm{p}}'(x)$ for both, the hard and soft magnets in Fig. 3a and b, which clearly shows that f_{soft}' approaches $+\infty$ slower than f_{hard}'. This property, in turn, yields a more "gradual" saturation in the hard magnets as compared to the soft magnetic

[5] The function is chosen such that $f_{\mathrm{soft}}'(x)$ becomes $f_{\mathrm{soft}}'(x)=x+0.067x^2\sin(3.5x)+0.33x^3/(1-x)$, which is the approximate inverse Langevin function proposed by Petrosyan (2016).

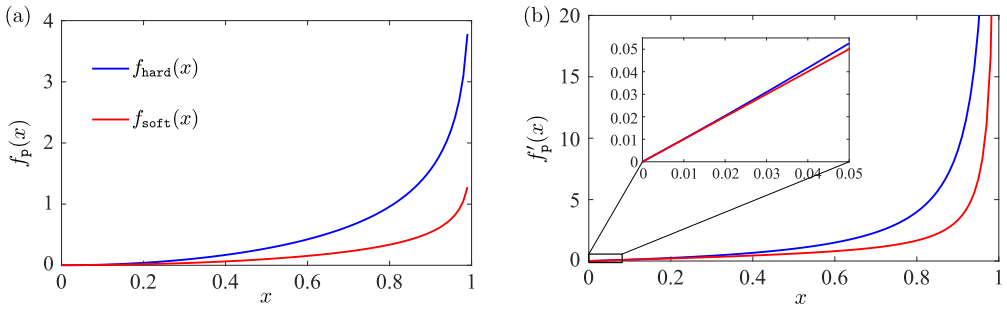

Fig. 3. Comparison of the (a) hardening functions $f_{\text{p}}(x)$ and (b) their derivatives $f'_{\text{p}}(x)$ for the and soft magnetic particles.

Table 1
Magnetic properties of the particles.

	χ^e_{p}	χ^r_{p}	$\mu_0 m^s_{\text{p}}$ (T)	b^c_{p} (T)	μ_0 ($\mu\text{N}\cdot\text{A}^{-2}$)
NdFeB (hard)	0.105	8.0	0.84	1.062	$4\pi 10^{-1}$
Carbonyl iron (soft)	0.0	30.0	2.5	0.001	$4\pi 10^{-1}$

counterpart. Nevertheless, the initial slope near $x = 0$ remains the same for both f'_{hard} and f'_{soft}, thus, ensuring the same initial susceptibility of χ^r_{p} given $\chi^e_{\text{p}} = 0$.[6]

Once the hardening function is selected, we calibrate the coercivity, susceptibilities and the saturation magnetization parameters from available experimental data by fitting the model response employing a least square-based fitting algorithm (see Mukherjee and Danas (2019) for details). These calibrated parameters for the NdFeB and iron particles are given in Table 1.

4.3. Computation of the local model response

The local magnetization and magnetostriction (strain induced by the local particle-to-particle interactions in the composite) responses are obtained from the proposed constitutive models via solving for the stretch components λ_i $(i = 1-3)$ and the magnetic primary variable (**H** or **B** depending on the model) components from the equations

$$S_{11} - S^{\text{maxw}}_{11} = S_{22} - S^{\text{maxw}}_{22} = S_{33} - S^{\text{maxw}}_{33} = 0 \qquad \text{and} \qquad h_1 - h^a = h_2 = 0, \tag{4.5}$$

where $\mathbf{h}^a$ is the applied Eulerian h-field. Moreover, we consider $F_{ij} = 0$ for all $i \neq j$ in this particular case of uniaxial loading/unloading. Specifically, we consider a purely magnetic uniaxial loading along $\mathbf{e}_1$. The variation of h_1 with time is considered to be a simple ramp-type increase to the maximum h_1 and subsequently decrease to the minimum h_1. However, the temporal profile of the magnetic loading remains inconsequential in the proposed rate-independent MRE models. The evolution of the internal variable ξ is computed numerically solving (3.15) with a fully implicit Newton–Raphson solution method (see Chapter 4 of Mukherjee (2020) for details).

We emphasize that the Maxwell stress $\mathbf{S}^{\text{maxw}}$ must be subtracted from the total stress **S** to capture the actual magneto-mechanical coupling at the material level. A detailed explanation for this manipulation is provided by Danas (2017) and Mukherjee et al. (2021) in the context of s- and h-MREs, respectively. Thus, in this text we refrain from discussing any further details on the significance of (4.5) for brevity. In particular, we use the relevant expressions for $\mathbf{S}^{\text{maxw}}$ as provided in Section 2.4 in the context of **F**−**H** and **F**−**B**-based constitutive modeling.

[6] The function $f_{\text{soft}}(x)$ in (4.4) does not reduce exactly to $0.5x^2 + \mathcal{O}(x^3)$ in its Taylor series expansion. Nevertheless, Fig. 3b shows that the slopes of f'_{soft} and f'_{hard} remain nearly the same near $x = 0$. Moreover, both functions yield a qualitatively similar overall behavior.

4.4. Calibration for the coupling β parameter

The proposed **F**−**H** and **F**−**B** model responses are compared with the full-field numerical homogenization response in Fig. 4 for $c = 0.1,\ 0.2$ and 0.3. Here we consider a representative $G_{\text{m}} = 0.5$ MPa, which corresponds to the shear modulus of the PDMS elastomer. Notice in Fig. 4a that the saturation magnetization of the h-MREs increases in an almost linear fashion with c, which resembles closely to the s-MREs responses (Lefère and Lopez-Pamies, 2017; Danas, 2017; Mukherjee et al., 2020). The coercivity b^c of the composite, however, undergoes very little change with the increase in c. Nonetheless, the effective susceptibilities χ^e and χ^r also increase with c, which can be observed clearly from Fig. 4a. Overall, the model predictions for the magnetization in the h-MRE match perfectly with the numerically computed effective response.

The local magnetostriction responses, on the other hand, exhibit a butterfly-shaped hysteresis loop with the applied cyclic magnetic field (see Fig. 4b and c). This response is essentially controlled by the coupling parameter β, which is calibrated from the numerically computed magnetostriction responses to be

$$\beta = 19.0c^2 - 10.4c + 1.71 \tag{4.6}$$

by considering the proposed **F** − **H** model (Mukherjee et al., 2021). Being the closed form complementary energy density, the **F** − **B** model does not need any further calibration. Thus, the same β parameter is used for the **F** − **B** model, yielding excellent match with the numerical homogenization response.

4.5. Soft MRE model response

Finally, we probe the calibrated model response against another set of numerically computed effective response but now for the case of s-MREs with carbonyl iron particle inclusions. Specifically, we consider a $G_{\text{m}} = 0.3$ MPa along with the soft magnetic particle parameters shown in Table 1 and the coupling parameter as in (4.6). The microscopic computations of the effective response for this particular case is detailed in Mukherjee et al. (2020).

We plot the numerical FE response from Mukherjee et al. (2020) along with the model magnetization and magnetostriction responses in Fig. 5a and b, c, respectively. Besides the excellent agreement between the numerical homogenization computations and the model predictions, we observe two key differences between the s- and h-MREs by comparing Figs. 4 and 5. Firstly, and the obvious is the absence of hysteresis in the s-MREs. Moreover, the latter tends to saturate at a lower applied h_1, while the former never saturates to a constant magnetization.

5. Time discrete variational principles — solution of the boundary value problems

The rate-type variational principles for the **F** − **H** and **F** − **B** models in Section 2 are now expressed in a time discrete form to analyze

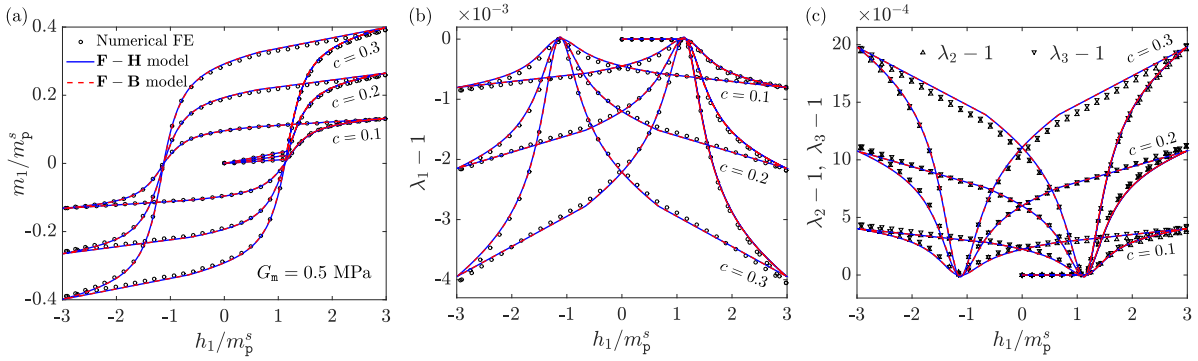

Fig. 4. Comparison of the local (a) magnetization, (b) parallel and (c) transverse magnetostriction responses from the $\mathbf{F}-\mathbf{H}$ and $\mathbf{F}-\mathbf{B}$ models with the numerical homogenization estimates. The h-MRE is subjected to an uniaxial cyclic h-field of magnitude $|h_1| = 3m_{\mathrm{p}}^s$ and the results for three different particle volume fractions of $c = 0.1,\ 0.2$ and 0.3 are shown.

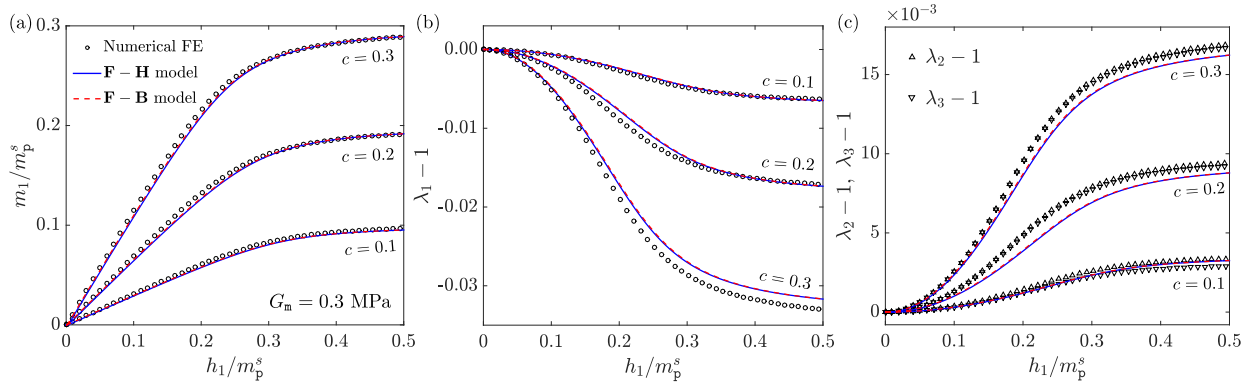

Fig. 5. Comparison of the local (a) magnetization, (b) parallel and (c) transverse magnetostriction responses from the $\mathbf{F}-\mathbf{H}$ and $\mathbf{F}-\mathbf{B}$ models with the numerical homogenization estimates. The s-MRE is subjected to an uniaxial cyclic h-field of magnitude $|h_1| = 0.5m_{\mathrm{p}}^s$ and the results for three different particle volume fractions of $c = 0.1,\ 0.2$ and 0.3 are shown.

any practical boundary value problem (BVP) involving MREs. First, the scalar potential-based $\mathbf{F}-\mathbf{H}$ model is present in a time discrete form. This will be followed by the specification of the corresponding vector potential-based $\mathbf{F}-\mathbf{B}$ model.

5.1. Time discrete variational principle for $\mathbf{F}-\mathbf{H}$ model

The scalar potential-based $\mathbf{F}-\mathbf{H}$ model needs to be solved for the displacement $\mathbf{u}$ and potential φ, such that $\mathbf{F} = \mathbf{I} + \mathrm{Grad}\mathbf{u}$ and $\mathbf{H} = -\mathrm{Grad}\varphi$ both satisfy the relevant Dirichlet boundary conditions. Specifically in the incremental setting of a numerical solution, we consider the state of the continuum to be known at a time t, from which we solve for the minimizing fields $\mathbf{u}$ and φ for the next time step $\tau = t + \Delta t$. We henceforth indicate all the variables with the subscripts "t" or "τ" to indicate that the variables are computed at a given discrete time.

First, the variational principle (2.3) upon substitution of $D(\dot{\boldsymbol{\xi}})$ from (3.14) reads

$$\dot{\Pi}^{\mathrm{H}} = \inf_{\dot{\mathbf{u}}\in\widetilde{\mathcal{U}}} \sup_{\dot{\varphi}\in\widetilde{\mathcal{G}}} \inf_{\dot{\boldsymbol{\xi}}\in\mathbb{R}^3} \left[\int_{\mathbb{R}^3} \dot{W}^{\mathrm{H}}(\mathbb{C},\mathbf{H},\dot{\boldsymbol{\xi}})\,\mathrm{d}\mathcal{V}_0 - \int_{\partial\mathcal{V}_0} \mathbf{T}\cdot\dot{\mathbf{u}}\,\mathrm{d}\mathcal{S}_0 + \int_{\mathcal{V}_0} \sup_{\boldsymbol{\eta}} \inf_{\dot{\Lambda}\geq 0} \left\{ \boldsymbol{\eta}\cdot\dot{\boldsymbol{\xi}} - \dot{\Lambda}\Phi(\boldsymbol{\eta}) \right\} \mathrm{d}\mathcal{V}_0 \right]. \tag{5.1}$$

Expressing all the rates in time discrete form like $\dot{\mathbf{u}} = (\mathbf{u}_\tau - \mathbf{u}_t)/\Delta t$ and taking note on the fact that the state at time t is already converged, one can express the rate-type variational principle (5.1) in a time-discrete form so that

$$\Pi_\tau^{\mathrm{H}} = \inf_{\mathbf{u}_\tau\in\mathcal{U}} \sup_{\varphi_\tau\in\mathcal{G}} \left[\int_{\mathcal{V}_0} \mathcal{W}_\tau^{\mathrm{H}}(\mathbb{C},\mathbf{H})\,\mathrm{d}\mathcal{V}_0 + \int_{\mathbb{R}^3\setminus\mathcal{V}_0} W_{c=0,\tau}^{\mathrm{H}}(\mathbb{C},\mathbf{H})\,\mathrm{d}\mathcal{V}_0 - \int_{\partial\mathcal{V}_0} \mathbf{T}\cdot\mathbf{u}_\tau\,\mathrm{d}\mathcal{S}_0 \right]. \tag{5.2}$$

Here the subscript "τ" with W^{H} and $\mathcal{W}^{\mathrm{H}}$ both indicate that all their arguments are at a discrete time τ. In (5.2) we have introduced a *reduced energy density* $\mathcal{W}_\tau^{\mathrm{H}}$, which is, in turn, the variational principle employed for the computation for the internal variable $\boldsymbol{\xi}_\tau$ locally at each point of the computation domain, such that

$$\mathcal{W}_\tau^{\mathrm{H}}(\mathbb{C},\mathbf{H}) = \inf_{\boldsymbol{\xi}_\tau} \sup_{\boldsymbol{\eta}} \inf_{\Delta\Lambda\geq 0} \left\{ W_\tau^{\mathrm{H}}(\mathbb{C},\mathbf{H},\boldsymbol{\xi}) + \boldsymbol{\eta}\cdot\boldsymbol{\xi}_\tau - \Delta\Lambda\Phi(\boldsymbol{\eta}) \right\}. \tag{5.3}$$

This last variational statement, in turn, leads to the time-discrete forms of the KKT conditions stated in (3.15). Finally, the admissible sets for $\mathbf{u}_\tau$ and φ_τ are given by, respectively,

$$\mathcal{U} \equiv \left\{ \mathbf{u}_\tau :\ \mathbf{F}_\tau = \mathbf{I}+\mathrm{Grad}\mathbf{u}_\tau,\ J_\tau > 0,\ \forall\,\mathbf{X}\in\mathbb{R}^3 \text{ and } \mathbf{u}_\tau = \overline{\mathbf{u}}_\tau,\ \forall\,\mathbf{X}\in\partial V_0^{\mathbf{u}} \right\}, \tag{5.4}$$

$$\mathcal{G} \equiv \left\{ \varphi_\tau :\ \mathbf{H}_\tau = -\mathrm{Grad}\varphi_\tau,\ \forall\,\mathbf{X}\in\mathbb{R}^3 \text{ and } \varphi_\tau = \overline{\varphi}_\tau,\ \forall\,\mathbf{X}\in\partial V_\infty^{\varphi} \right\}. \tag{5.5}$$

Thus, for an initial guess $\mathbf{u}_\tau$ and φ_τ we first update the internal variable $\boldsymbol{\xi}_\tau$ via extremizing (5.3). Then the updated $\boldsymbol{\xi}_\tau$ is used to compute for the corrector for $\mathbf{u}_\tau$ and φ_τ from the global implicit solver. Thus, the introduction of the reduced energy density allows us to update $\boldsymbol{\xi}_\tau$ locally at each integration point, while computing for $\mathbf{u}_\tau$ and φ_τ from the global variational principle. This computation algorithm provides efficient update procedure for $\mathbf{u}$, φ and $\boldsymbol{\xi}$ and facilitates the implementation in the commercially-available finite-element solvers like ABAQUS/Standard (Miehe et al., 2011; Rosato and Miehe, 2014; Mukherjee et al., 2021).

5.2. Time discrete variational principle for $\mathbf{F}-\mathbf{B}$ model

The time discrete equivalent of the $\mathbf{F}-\mathbf{B}$-based variational principle (2.12) can be obtained in a similar way to (5.2) after substituting $D(\xi)$ from (3.14), finally leading to

$$\Pi_\tau^{\mathrm{B}} = \inf_{\mathbf{u}_\tau\in\mathcal{U}} \inf_{\mathbf{A}_\tau\in\mathcal{B}} \left[\int_{\mathcal{V}_0} \mathcal{W}_\tau^{\mathrm{B}}(\mathbb{C},\mathbf{B})\, \mathrm{d}\mathcal{V}_0 + \int_{\mathbb{R}^3\setminus\mathcal{V}_0} W_{c=0,\tau}^{\mathrm{B}}(\mathbb{C},\mathbf{B})\, \mathrm{d}\mathcal{V}_0 - \int_{\partial\mathcal{V}_0} \mathbf{T}\cdot\mathbf{u}_\tau\, \mathrm{d}S_0 \right], \tag{5.6}$$

where the reduced energy density $\mathcal{W}_\tau^{\mathrm{B}}(\mathbb{C},\mathbf{B})$ reads

$$\mathcal{W}_\tau^{\mathrm{B}}(\mathbb{C},\mathbf{B}) = \inf_{\xi_\tau} \sup_{\boldsymbol{\eta}} \inf_{\Delta\Lambda\geq 0} \left\{ W_\tau^{\mathrm{B}}(\mathbb{C},\mathbf{B},\xi) + \boldsymbol{\eta}\cdot\xi_\tau - \Delta\Lambda\Phi(\boldsymbol{\eta}) \right\}. \tag{5.7}$$

Again, the extremization of (5.7) leads to the KKT conditions for the $\mathbf{F}-\mathbf{B}$ model and thus, to the update equations for ξ_τ. The admissible set $\mathcal{U}$ for the displacement field remains the same as in (5.4), while the admissible set for the vector potential $\mathbf{A}_\tau$ reads

$$\mathcal{B} \equiv \left\{ \mathbf{A}_\tau :\ \mathbf{B}_\tau = \mathrm{Curl}\,\mathbf{A}_\tau,\ \mathrm{Div}\,\mathbf{A}_\tau = 0,\ \forall\,\mathbf{X}\in\mathbb{R}^3 \text{ and } \mathbf{A}_\tau = \overline{\mathbf{A}}_\tau,\ \forall\,\mathbf{X}\in\partial V_0^{\mathbf{A}} \right\}, \tag{5.8}$$

where the condition $\mathrm{Div}\,\mathbf{A}_\tau = 0$ is the well-known Coulomb gauge that leads to an uniquely defined vector potential $\mathbf{A}_\tau$ (Biro and Preis, 1989; Stark et al., 2015). The implementation of the Coulomb gauge may be done in various manners. Here, we use a penalty formulation described in Dorn et al. (2021) together with under-integration of the constraint term. Again, for an initial guess of $\mathbf{u}_\tau$ and $\mathbf{A}_\tau$, the internal variable ξ_t is updated to be ξ_τ at the local integration points. The subsequent global increments for the $\mathbf{u}_\tau$ and $\mathbf{A}_\tau$ are carried out via using the *already updated* ξ_τ. The correction increments for $\mathbf{u}_\tau$ and $\mathbf{A}_\tau$ continues until a global convergence is achieved.

5.3. Numerical BVP setting

The discretization of the scalar and vector potential-based variational principles were discussed in a fairly general setting so far in the last two subsections. We now specify a geometry for the numerical BVP of interest. Although the *h*-MREs are finding applications in a wide variety of engineering devices, such as in sensors, most of the recent attention is in fabrication and testing of pre-magnetized slender structures, which find applications in soft robotic devices (Kim et al., 2018; Zhao et al., 2019; Ren et al., 2019; Alapan et al., 2020). Thus, in this paper we will focus on various aspects of the bending of pre-magnetized slender beams under applied actuating magnetic fields. This includes spatially uniformly and non-uniformly pre-magnetized beams and functionally graded beams with a distribution of the particle volume fractions c.

In particular, we consider a two-dimensional, plane-strain analysis of the bending of pre-magnetized slender beams. We emphasize in this context, that the magnetic fields are applied via the fixed electromagnet poles far away from the MRE (not modeled explicitly here), both during the pre-magnetization and actuation. Thus, it is necessary to embed the MREs in a surrounding air. Moreover, since the magnetic fields are applied far away, the air domain is considered to be substantially larger than the MRE. In particular, we consider the air domain length $L = 10\ell$ to ensure that the MRE deflection is sufficiently far from the boundary of the air $\partial\mathcal{V}_{\mathrm{Air}}^{\mathrm{Top}} \cup \partial\mathcal{V}_{\mathrm{Air}}^{\mathrm{Right}} \cup \partial\mathcal{V}_{\mathrm{Air}}^{\mathrm{Bottom}} \cup \partial\mathcal{V}_{\mathrm{Air}}^{\mathrm{Left}}$ (see Fig. 6a).

As shown in Fig. 6b, the slender MRE beam of length ℓ and width w has a common interface $\partial\mathcal{V}_{\mathrm{MRE}}^{\mathrm{Top}} \cup \partial\mathcal{V}_{\mathrm{MRE}}^{\mathrm{Right}} \cup \partial\mathcal{V}_{\mathrm{MRE}}^{\mathrm{Bottom}} \cup \partial\mathcal{V}_{\mathrm{MRE}}^{\mathrm{Left}}$ with the surrounding air. The aspect ratio of the beam is hence defined via $r_{\mathrm{asp}} = \ell/w$. Finally, the structured FE mesh used in the computations is shown in Fig. 6c. Throughout this paper we consider linear four-node quadrilateral isoparametric elements in the FE computations.

5.4. Treatment of air

The air surrounding the MRE has (nearly) zero mechanical stiffness, whereas the magnetic $\mathbf{b}$ and $\mathbf{h}$ fields in it are finite. Specifically, the former is related to the latter via $\mathbf{b} = \mu_0\mathbf{h}$ in the surrounding air. Dealing with a material of nearly zero mechanical stiffness in the present fully implicit, Lagrangian modeling framework leads to extreme mesh distortions at the corners of the MRE, eventually stopping the numerical simulation from converging.

Till this date, a number of methods have been implemented for dealing with the surrounding air in the magneto-active structures. The most straightforward way to model the air is to consider it a nearly incompressible or compressible hyperelastic solid having shear modulus of ~1 Pa (Rambausek and Keip, 2018; Dorn et al., 2021). However, such an assumption may lead to an underestimation of the mechanical deformations of the MREs, specifically when undergoing large deformations or deflections. An alternative approach, namely, the method of constraining the motion of the air nodes surrounding the MRE is found to yield very accurate results of MRE deformations in air (Psarra et al., 2019; Mukherjee et al., 2021). In particular, the latter considers the air shear modulus to be zero but simultaneously applies linear constraints on each nodes in the air domain to make them move according to the deformation/deflection of the MRE boundary. Having said that, we also remark that the application of such linear constraints on the air nodes where two or more (magnetic or non-magnetic) structures are interacting may become difficult to implement properly so that numerical convergence is achieved. A quantitative comparison of the performance of different modeling approaches for the surrounding air is drawn in a companion paper (Rambausek et al., 2022).

In this paper, we consider standalone MRE beams that are subjected to spatially uniform magnetic fields, as shown in Fig. 6a. Thus, we employ the air node constraining method to model the deformation in the domain $\mathcal{V}_{\mathrm{Air}}$. In fact, the linear constraints on the displacement field $\mathbf{u}$ for all $\mathbf{X}\in\mathcal{V}_{\mathrm{Air}}$ can be applied via directly augmenting the incremental variational principles (5.2) and (5.6) by a penalty potential

$$W_{\mathtt{penalty}}(\mathbf{u}) = \sum_{j=1}^{N_{\mathrm{Air}}} \sum_{i=1}^{2} \frac{G_{\mathrm{c}}}{2L_{\mathrm{c}}\zeta} \left(C_i^{(j)} \right)^2, \tag{5.9}$$

where N_{Air} is the number of air nodes, L_{c} is a reference length parameter usually considered to be equal to w, G_{c} is an arbitrary shear modulus that we consider to be identical to that of the matrix and ζ is the penalty parameter, which is set to 10^{-3}. Nevertheless, any value of ζ in the range 10^{-6}–10^{-3} ensures a proper imposition of the constraint properly, not affecting the numerical convergence significantly. Given that those constraints are linear one has also the option to directly use the `*Equation` command in Abaqus. Such an approach has also been tested showing no differences with the penalty approach described here in two and three dimensions. Finally, the pointwise constraint $C_i^{(j)}$ is defined as (Psarra et al., 2019)

$$C_i^{(j)} \equiv \begin{cases} d_i^{(j)} u_i^{(j)}\big|_{\partial\mathcal{V}_{\mathrm{MRE}}} - u_i^{(j)}\big|_{\mathcal{V}_{\mathrm{Air}}} = 0, & \text{if } \ 0 < d_i^{(j)} \leq 1 \\ u_i^{(j)}\big|_{\mathcal{V}_{\mathrm{Air}}} = 0, & \text{otherwise,} \end{cases} \tag{5.10}$$

which constrains the displacement of any node j in $\mathcal{V}_{\mathrm{Air}}$ with that of it nearest node on the Air/MRE interface $\partial\mathcal{V}_{\mathrm{MRE}}$. In practice, we construct a set of two-node elements comprising one node from $\mathcal{V}_{\mathrm{Air}}$ and one from the set $\partial\mathcal{V}_{\mathrm{MRE}}$ that has the least Euclidean distance from the former. Subsequently, we add the "force" and "stiffness" terms to the global force and stiffness matrices. Those terms emerge by considering first and second variations of the corresponding degrees-of-freedom involved the penalty potential (5.9).

The constraint "weight" function $d_i^{(j)}$ is defined in terms of the absolute distance difference between the X_i $(i = 1, 2)$ coordinates of

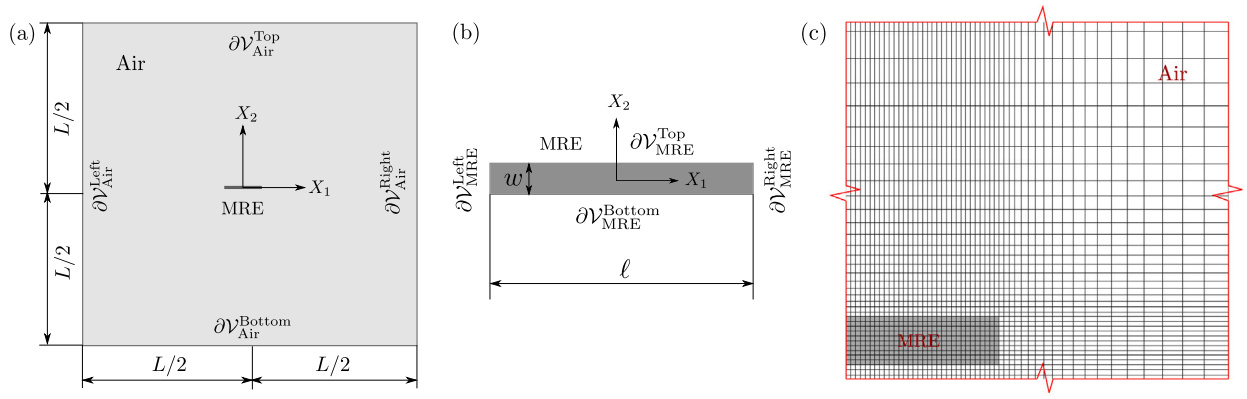

Fig. 6. (a) Diagram of the full BVP domain having MRE and the surrounding air. The air domain with an external boundary $\partial\mathcal{V}_{\text{Air}}^{\text{Top}} \cup \partial\mathcal{V}_{\text{Air}}^{\text{Right}} \cup \partial\mathcal{V}_{\text{Air}}^{\text{Bottom}} \cup \partial\mathcal{V}_{\text{Air}}^{\text{Left}}$ is considered to be a square of length L. The reference coordinate system $\mathbf{X}$ is considered to have origin at the center of the air domain. (b) Dimensions of the MRE having the interface $\partial\mathcal{V}_{\text{MRE}}^{\text{Top}} \cup \partial\mathcal{V}_{\text{MRE}}^{\text{Right}} \cup \partial\mathcal{V}_{\text{MRE}}^{\text{Bottom}} \cup \partial\mathcal{V}_{\text{MRE}}^{\text{Left}}$ with the surrounding air. The MRE length ℓ is considered to be $\ell = 0.1L$ and the aspect ratio of the MRE is defined as $r_{\text{asp}} = \ell/w$. (c) A part of the structured mesh considered in the calculations. Standard linear 4-node quadratic isoparametric elements are employed.

the points in $\mathcal{V}_{\text{Air}}$ and on $\partial\mathcal{V}_{\text{MRE}}$, such that

$$d_i^{(j)} = 1 - \frac{\left|X_i^{(j)}\right|_{\mathcal{V}_{\text{Air}}} - X_i^{(j)}\Big|_{\partial\mathcal{V}_{\text{MRE}}}\Big|}{0.5L}, \qquad \text{with} \quad i = 1, 2. \tag{5.11}$$

With (5.9) along with the BVP definition in Fig. 6, the $\mathbf{F}-\mathbf{H}$-based incremental variational principle (5.2) reads

$$\Pi_\tau^{\text{H}} = \inf_{\mathbf{u}_\tau \in \mathcal{U}} \sup_{\varphi_\tau \in \mathcal{G}} \left[\int_{\mathcal{V}_{\text{MRE}}} \mathcal{W}_\tau^{\text{H}}(\mathbb{C}, \mathbf{H})\, \mathrm{d}\mathcal{V}_0 + \int_{\mathcal{V}_{\text{Air}}} W_{c=0,\tau}^{\text{H}}(\mathbb{C}, \mathbf{H})\, \mathrm{d}\mathcal{V}_0 + W_{\text{penalty}}(\mathbf{u}_\tau) \right]. \tag{5.12}$$

Even though the specific Dirichlet boundary conditions for the $\mathbf{u}$ and φ fields change depending on the loading conditions, the general form of the admissible sets $\mathcal{U}$ and $\mathcal{G}$ remains the same as in (5.4) and (5.5), respectively. Similarly, the $\mathbf{F}-\mathbf{B}$ incremental variational principle now reads

$$\Pi_\tau^{\text{B}} = \inf_{\mathbf{u}_\tau \in \mathcal{U}} \inf_{\mathbf{A}_\tau \in \mathcal{B}} \left[\int_{\mathcal{V}_{\text{MRE}}} \mathcal{W}_\tau^{\text{B}}(\mathbb{C}, \mathbf{B})\, \mathrm{d}\mathcal{V}_0 + \int_{\mathcal{V}_{\text{Air}}} W_{c=0,\tau}^{\text{B}}(\mathbb{C}, \mathbf{B})\, \mathrm{d}\mathcal{V}_0 + W_{\text{penalty}}(\mathbf{u}_\tau) \right], \tag{5.13}$$

where the admissible set $\mathcal{B}$ for the vector potential $\mathbf{A}_\tau$ is given by

$$\mathcal{B} \equiv \Big\{ \mathbf{A}_\tau \,:\, \mathbf{B}_\tau = \text{Curl}\mathbf{A}_\tau,\ \mathbf{A}_\tau(X_1, X_2) = \alpha_\tau(X_1, X_2)\hat{\mathbf{E}}_3 \quad \forall\, \mathbf{X} \in \mathcal{V}_{\text{MRE}} \cup \mathcal{V}_{\text{Air}} \ \text{and} \alpha_\tau = \alpha_\tau^a,\ \forall\, \mathbf{X} \in \partial V_{\text{Air}} \Big\}. \tag{5.14}$$

Notice that for the present 2D plane strain analysis, we consider only the out of plane $\hat{\mathbf{E}}_3$ component of the vector potential $\mathbf{A}_\tau$, so that the components of $\mathbf{B}_\tau$ are given by $(B_\tau)_i = \epsilon_{ij}(\alpha_\tau)_{,i}$, where ϵ_{ij} is the 2D permutation symbol (Psarra et al., 2017; Danas, 2017). In this case no Coulomb gauge is required. For a three-dimensional implementation of the Coulomb gauge the reader is referred to Dorn et al. (2021).

6. Results

This section shows numerically computed BVP solutions for uniformly and non-uniformly pre-magnetized h-MRE beams, s-MRE beams and the cantilever beams having h-/s-MRE laminated structures. The following results consider the hard/soft particle magnetization parameters as in Table 1 and the matrix shear modulus is taken to be $G_{\text{m}} = 0.187$ MPa, which resembles closely to that of the moderately-soft PDMS elastomers (Kim et al., 2018; Zhao et al., 2019). Moreover, the matrix bulk modulus is considered to be $G'_{\text{m}} = 500G_{\text{m}}$, which ensures a *nearly incompressible* material response. The particle volume fraction c and the loading conditions for the pre-magnetization and actuation steps are discussed under specific subsections depending on the examples. Moreover, the specific Dirichlet boundary conditions on $\mathbf{u}_\tau$, φ_τ and α_τ, i.e, the case-specific versions of the admissible sets $\mathcal{U}$, $\mathcal{G}$ and $\mathcal{B}$, respectively, are detailed in the following.

6.1. Uniformly pre-magnetized h-MRE cantilever beams

We start with the simplest case of the uniformly pre-magnetized cantilever beams with the aspect ratios $r_{\text{asp}} = 10$ and 17.5. Specifically, we simulate the experimental observations of Zhao et al. (2019) for the deflection of pre-magnetized h-MREs under uniform transverse actuation fields. To accomplish that, the loading is considered to be two steps, which are detailed in the following.

- `Step-I`: First, we carry out the pre-magnetization along $\hat{\mathbf{E}}_1$ by considering the air and MRE boundaries to be fixed. Thus, the Dirichlet boundary conditions on $\mathbf{u}$ and φ for the $\mathbf{F}-\mathbf{H}$ model reads

$$\mathbf{u}_\tau = \mathbf{0}, \quad \forall\, \mathbf{X} \in \partial\mathcal{V}_{\text{MRE}}, \quad \text{and} \quad \mathbf{u}_\tau = \mathbf{0}, \quad \forall\, \mathbf{X} \in \partial\mathcal{V}_{\text{Air}} \tag{6.1}$$

$$\varphi_\tau = 0, \quad \forall\, \mathbf{X} \in \partial\mathcal{V}_{\text{Air}}^{\text{Left}} \quad \text{and} \quad \varphi_\tau = -\frac{b_{1,\tau}^{\text{mag}}}{\mu_0} L, \quad \forall\, \mathbf{X} \in \partial\mathcal{V}_{\text{Air}}^{\text{Left}}, \tag{6.2}$$

  where $b_{1,\tau}^{\text{mag}}$ is the magnetization field at time τ. In particular, $b_{1,\tau}^{\text{mag}}$ is increased linearly in time up to 2 T followed by its decrease at the same rate to 0 T. The rate of $b_{1,\tau}^{\text{mag}}$ (and all the following applied fields) is inconsequential in the simulations since the material model is rate-independent. Similarly, the Dirichlet boundary condition on α for the $\mathbf{F}-\mathbf{B}$ model reads

$$\alpha_\tau = 0, \quad \forall\, \mathbf{X} \in \partial\mathcal{V}_{\text{Air}}^{\text{Bottom}} \quad \text{and} \quad \alpha_\tau = b_{1,\tau}^{\text{mag}} L, \quad \forall\, \mathbf{X} \in \partial\mathcal{V}_{\text{Air}}^{\text{Top}}, \tag{6.3}$$

  while that on $\mathbf{u}_\tau$ remains identical to (6.1).
- `Step-II`: Next, we carry out the actuation step, where we apply a uniform field b_2^{actu} along $\hat{\mathbf{E}}_2$, i.e., transverse to the centerline of the beam. The magnitude of b_2^{actu} is increased monotonically from 0 T. The specific Dirichlet boundary conditions on $\mathbf{u}_\tau$ and φ_τ in this step for the $\mathbf{F}-\mathbf{H}$ model reads

$$\mathbf{u}_\tau = \mathbf{0}, \quad \forall\, \mathbf{X} \in \partial\mathcal{V}_{\text{MRE}}^{\text{Left}}, \quad \text{and} \quad \mathbf{u}_\tau = \mathbf{0}, \quad \forall\, \mathbf{X} \in \partial\mathcal{V}_{\text{Air}} \tag{6.4}$$

$$\varphi_\tau = 0, \quad \forall\, \mathbf{X} \in \partial\mathcal{V}_{\text{Air}}^{\text{Bottom}} \quad \text{and} \quad \varphi_\tau = -\frac{b_{2,\tau}^{\text{actu}}}{\mu_0} L, \quad \forall\, \mathbf{X} \in \partial\mathcal{V}_{\text{Air}}^{\text{Top}}. \tag{6.5}$$

  In turn, the boundary condition on α in this step for the $\mathbf{F}-\mathbf{B}$ model computations reads

$$\alpha_\tau = 0, \quad \forall\, \mathbf{X} \in \partial\mathcal{V}_{\text{Air}}^{\text{Left}} \quad \text{and} \quad \alpha_\tau = -b_{2,\tau}^{\text{actu}} L, \quad \forall\, \mathbf{X} \in \partial\mathcal{V}_{\text{Air}}^{\text{Right}}. \tag{6.6}$$

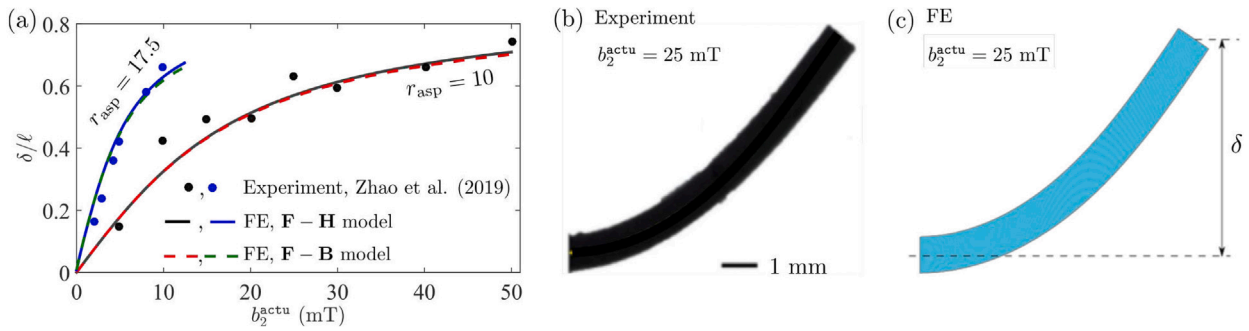

Fig. 7. (a) Comparison of the experimentally measured and the model (both **F** – **H** and **F** – **B**) predicted end-tip deflections of the pre-magnetized cantilever beams of $r_{asp} = 10$ and 17.5 under the applied actuation field along $\mathbf{e}_2$. Comparison of the FE predicted deflected beam shape with the respective experimental measurements of Zhao et al. (2019) under $b_2^{actu} = 25$ mT for (b) $r_{asp} = 10$ and (c) 17.5.

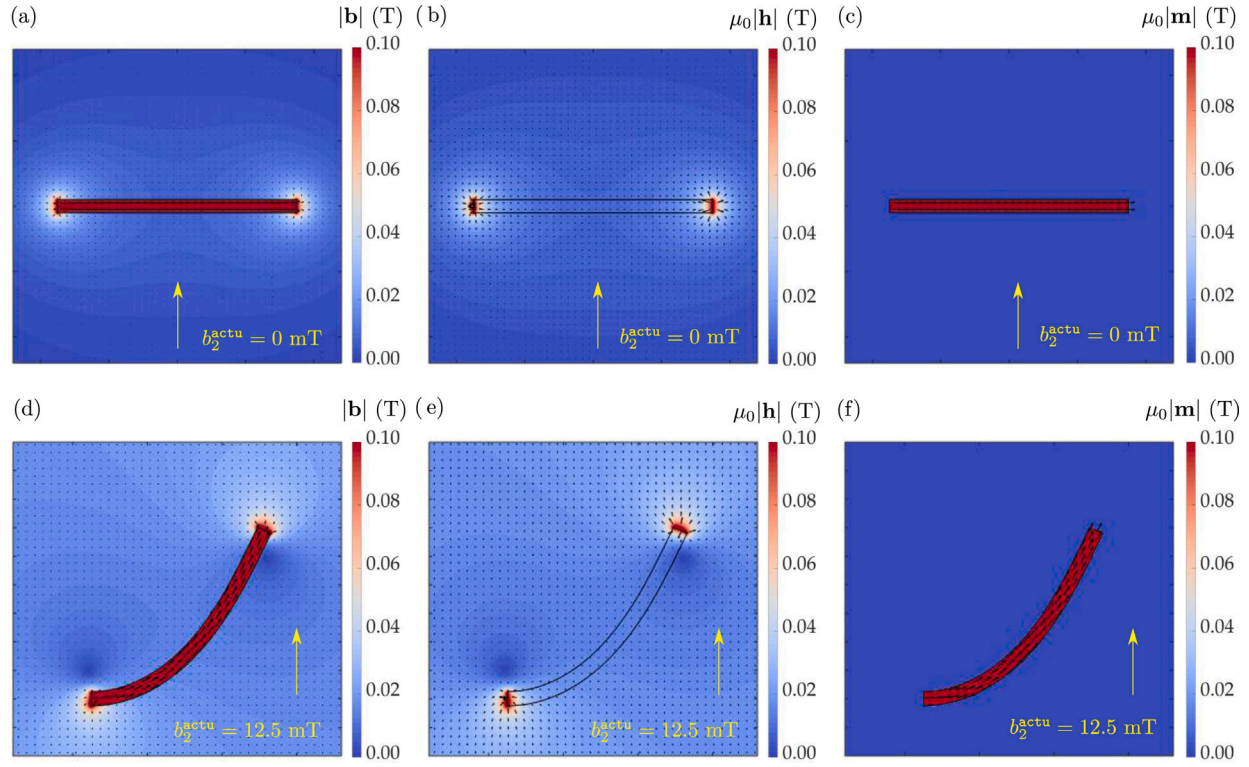

Fig. 8. Contours of the (a, (d) $|\mathbf{b}|$, (b, (e) $|\mathbf{h}|$ and (c, (f) $|\mathbf{m}|$ fields in and around a pre-magnetized h-MRE cantilever of $r_{asp} = 17.5$, (a–c) before and (d–f) after the application of an actuation field $b_2^{actu} = 12.5$ mT along $\hat{\mathbf{E}}_2$. The black colored arrows are used to indicate the direction of the respective vector fields. The length of the arrows are scaled according to the magnitude of the respective vectors.

In addition, we choose to work with a particle volume fraction of $c = 0.177$, which is identical to that of the fabricated h-MREs by Zhao et al. (2019). Moreover, we consider $G_m = 0.187$ MPa, which leads to an effective shear modulus $G = 0.303$ MPa for the composite. In fact, the latter is experimentally measured by Zhao et al. (2019) for the h-MREs with $c = 0.177$.

In agreement to the experimental observations, the computations show the pre-magnetized h-MREs to deflect immediately under the applied b_2^{actu}. The end-tip deflections of the pre-magnetized cantilevers with an increasing b_2^{actu} is plotted in Fig. 7a for $r_{asp} = 10$ and 17.5.

Therein, we observe that the **F** – **H** and **F** – **B**-based numerical simulations yield identical responses, which also agree with the experimentally measured end-tip deflection values for the two aforementioned aspect ratios. Moreover, the experimentally captured deflected shape in Fig. 7b, which is of the cantilever beam having $r_{asp} = 10$ under $b_2^{actu} = 25$ mT agrees excellently with its numerically computed counterpart in Fig. 7c. The FE solutions are carried out via writing an user-defined element (UEL) and coupling it with the ABAQUS/Standard solver.

The contours of the magnetic **b**, **h** and **m** field magnitudes along with the arrows showing their directions in and around the pre-magnetized h-MRE cantilever of $r_{asp} = 17.5$ are shown in Fig. 8. Specifically, we show the contours under $b_2^{actu} = 0$ mT and $b_2^{actu} = 12.5$ mT in Figs. 8a–c and d–f, respectively. Notice from Fig. 8b that the **h** field in the pre-magnetized cantilever is considerably smaller than the **b** and **m** fields in it. Thus, one can approximate the remanent b-field,i.e., the b-field in the h-MRE after pre magnetization as shown in Fig. 8a, to be $\mathbf{b}^r \approx \mu_0\mathbf{m}$. This is, in fact, the key feature upon which the magnetic torque-based models (Kim et al., 2018; Zhao et al., 2019) for the pre-magnetized h-MREs are based. Such simple approximations, however, do not hold in general for the cases of non-uniform pre-magnetization or the hybrid h-/s-MRE beams. Specific examples of the hybrid h-/s-MRE beams and non-uniform pre-magnetization will be discussed later in this section.

The contours in and around the deflected h-MRE under $b_2^{\texttt{actu}} = 12.5$ mT in Figs. 8d–f show that the magnetic self fields (both, **b** and **h** but not **m**, which is 0 in the air) around it get perturbed by the external field application and the mechanical deformation of the beam. The remanent **b** and **m** fields in the h-MRE, however, only undergo rotation with a negligible change in their magnitudes. Clearly, the applied field $b_2^{\texttt{actu}} = 12.5$ mT, which results in such a rapid deflection of the cantilever, is too weak to alter the remanent magnetization direction. Thus, in spite of being a dissipative material in general, such very low field deflections of the pre-magnetized beams leads to a highly reversible structural response, hence, making them an ideal candidate for the remotely-actuated soft robots (Ren et al., 2019; Alapan et al., 2020; Lucarini et al., 2022).

6.2. *s*-MRE cantilever beams under transverse magnetic field

Next, we consider the exact same loading conditions as in Section 6.1 but now with the soft magnetic carbonyl iron particles as the fillers. Identical to Section 6.1, we consider the particle volume fraction of $c = 0.177$ and a matrix shear modulus of $G_{\mathrm{m}} = 0.187$ MPa. Since Fig. 7a shows that the $\mathbf{F}-\mathbf{H}$ and $\mathbf{F}-\mathbf{B}$-based numerical simulations yield identical results, from here onwards we only show the results yielding from the $\mathbf{F}-\mathbf{H}$ model simulations.

Evidently, the pre-magnetization `Step-I` becomes inconsequential in this case, where the magnetic coercivity is vanishingly small. Nevertheless, the `Step-II`, i.e., the actuation step exhibit an interesting feature as shown in Fig. 9a. Firstly, there is no significant deflection in the low field actuation regime, i.e., $b_2^{\texttt{actu}} < 50$ mT. However, once $b_2^{\texttt{actu}}$ is increased beyond 0.2 T, we observe a rapid increase in the beam deflection such that the cantilever start to deflect and align itself momentarily with the applied $b_2^{\texttt{actu}}$ direction. Such an unstable, snapping-type response cannot be captured by the present fully implicit FE solver. Of course, the s-MRE cantilevers start becoming unstable at a lower $b_2^{\texttt{actu}}$ with the increasing r_{asp} as the flexural strength of the cantilever also decreases with the increasing r_{asp}.

The contours of the **b**, **h** and **m** field magnitudes along with their directions shown by the arrows in and around the s-MRE cantilever of $r_{\mathrm{asp}} = 17.5$ under $b_2^{\texttt{actu}} \approx 0.2$ T, i.e., at the last numerically converged state are shown in Fig. 9b–d, respectively. Since there was no remanent **b** and **m** before the application of $b_2^{\texttt{actu}}$, we observe in Fig. 9b–d that the local **b**, **h** and **m** fields remain always aligned to the direction of $b_2^{\texttt{actu}}$, thus, contrasting the observations for the h-MREs in Fig. 8. Indeed, this very low field responsiveness of the h-MREs makes them a better candidate for the soft robots as compared to the s-MREs. Nevertheless, s-MREs allow for a completely demagnetized behavior upon removal of the magnetic field, a feature that may be necessary in a numerous other applications such as cell-growth devices.

6.3. Pre-magnetized hybrid *h*-/*s*-MRE cantilever beams

Given the variety of applications of the pre-magnetized slender structures and the advancements in their fabrication techniques, one can come up with *functionally-graded* composite structures with domains of soft and hard magnetic fillers. In order to demonstrate the model applicability in all those application-oriented, hybrid MREs, we consider the slender cantilever beams with $r_{\mathrm{asp}} = 12$, having simple rank-1 laminates of h- and s-MREs. Specifically, we consider two sets of laminated structures as shown in Fig. 10a and b, i.e, having unit normals $\mathbf{n}_{\mathrm{lam}}$ on the laminate interfaces along $\widehat{\mathbf{E}}_2$ and $\widehat{\mathbf{E}}_1$, respectively. For simplicity, we refer to the former as the "horizontal" and the latter as the "vertical" laminates in the discussions to follow. All the laminates are considered to have uniform thickness of t_{lam}.

The pre-magnetization and actuation field amplitude and directions, along with the Dirichlet boundary conditions on $\mathbf{u}_r$ are considered to be identical to those defined in Section 6.1. Moreover, the particle volume fraction c and the matrix shear modulus G_{m} are also considered to be the same as in Section 6.1. Furthermore, the hard and soft magnetic particle properties are taken from Table 1. With these, the profile of the magnitude of remanent magnetization *after* the pre-magnetization step in the horizontally laminated beam along the cross section of the beam is shown in Fig. 10c, where three laminate thickness values, namely, $t_{\mathrm{lam}}/w = 0.5$, 0.25 and 0.125 are considered. As shown in Fig. 10c, the remanent magnetization in the h-MRE part remains $\sim cm_{\mathrm{p}}^s$, while that in the s-MRE part is vanishingly small. The direction of $\mathbf{m}^0$ remains along $\widehat{\mathbf{E}}_1$ in all the laminates.

In contrast, the pre-magnetized beam with vertical laminates exhibit a considerable amount of remanent magnetization in the s-MREs as well. In this context, Fig. 10d shows the variation of $|\mathbf{m}^0|$ along the centerline of the beam for three distinct cases with $t_{\mathrm{lam}}/\ell = 0.5$, 0.25 and 0.125. The direction of $\mathbf{m}^0$ remains identically along $\widehat{\mathbf{E}}_1$, i.e., the pre-magnetization direction. Furthermore, we observe that, unlike the horizontal laminates, $|\mathbf{m}^0|$ in the s-MRE domains are not constant in the vertical laminates. Rather, the *average* $|\mathbf{m}^0|$ in the s-MRE phases increases with the decreasing t_{lam}. The explanation for this observation is straightforward, that is, when a s-MRE is placed between two identically pre-magnetized s-MREs, a finite **b** field and hence, a magnetization **m** field is induced to the s-MREs in order to maintain the continuity of the **b** fields across the boundaries those are perpendicular to the pre-magnetization direction. Of course, such an induction is not possible when the h-/s-MRE interface is placed *parallel* to the pre-magnetization field, i.e, in the case of horizontally laminated beams.

The end-tip deflections of the horizontally and vertically laminated cantilevers are shown in Fig. 11a and b, respectively. The horizontally laminated cantilevers exhibit a greater deflection with the increase in the lamination, i.e., decrease in t_{lam}. However, the relative increase in the deflection remains minuscule in these laminates, as seen in Fig. 11a. The horizontally laminated cantilevers, on the other hand, exhibit a lower deflection for $t_{\mathrm{lam}}/\ell = 0.5$. However, the end-tip deflection does not increase with the further refinement in the lamination beyond $t_{\mathrm{lam}}/\ell = 0.25$ (see Fig. 11b).

The contours of **b**, **h** and **m** field magnitudes, along with arrows showing their directions are shown in Fig. 12a and b for the horizontally and vertically laminated cantilevers, respectively, both under $b_2^{\texttt{actu}} = 50$ mT. Very little qualitative change is observed between the contours around the deflected uniformly pre-magnetized h-MREs (Fig. 8b) and that around the horizontally laminated pre-magnetized MREs (Fig. 12a). Moreover, as observed from Fig. 12a, the s-MRE phases in the horizontally laminated MREs behave identical to non-active elastomeric phase that acts as a binding laminate between two h-MRE layers. The vertically laminated cantilevers, however, exhibit non-zero **b** and **m** fields in the s-MRE phases. Hence, the magnetic self-fields around the MRE cantilever becomes more intricate and distinct from those around the uniformly pre-magnetized h-MREs (cf., Figs. 8d and 12d). However, such a difference would become less with a further refinement of the laminate.

Overall, with the present choice of material parameters and particle volume fractions, the behavior of the pre-magnetized h-/s-MRE laminated structures in the low field actuation regime is primarily controlled by the h-MRE phase. Furthermore, an increase in the degree of lamination does not significantly change the actuation performance of these hybrid MRE structures. Nevertheless, the proposed structures and many others that can derive from those involve a large number of design parameters (e.g., volume fraction of particles, pre-magnetization amplitudes, more complex lamination or geometrical patterning) and such an endeavor is left for a future study.

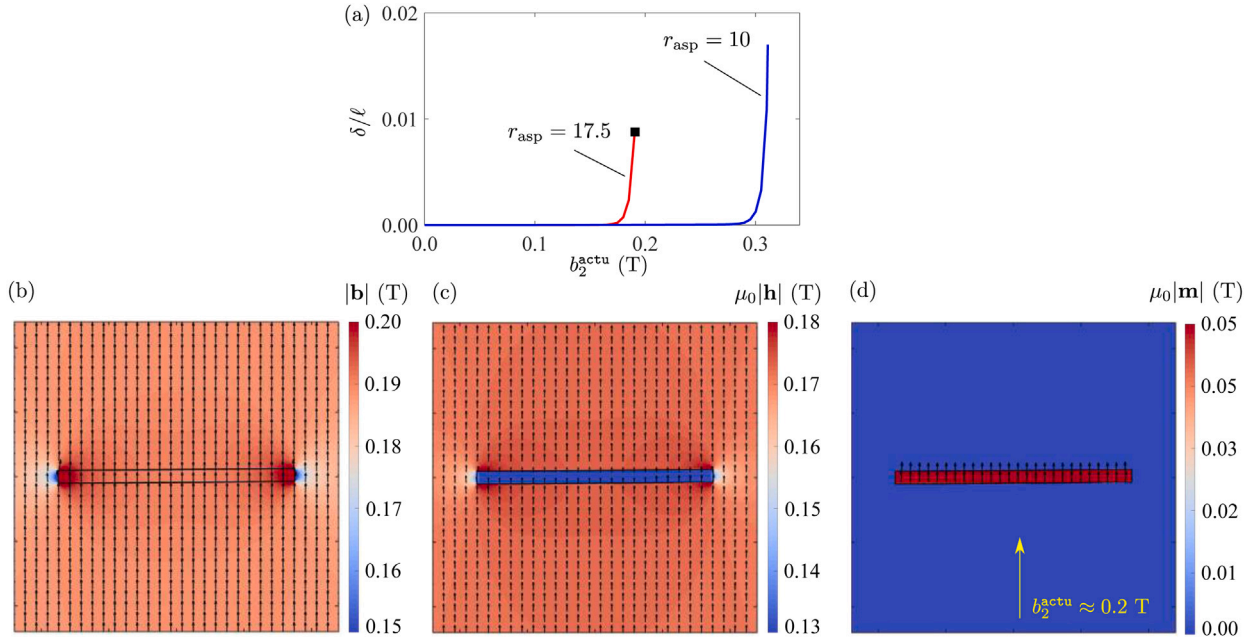

Fig. 9. (a) Variation of the end-tip deflection of the *s*-MREs of $r_{\text{asp}} = 10$ and 17.5 under the actuation field b_2^{actu} along $\widehat{\mathbf{E}}_2$. Contours of the (b) $|\mathbf{b}|$, (c) $|\mathbf{h}|$ and (d) $|\mathbf{m}|$ fields along with the respective directions of these vectors are shown in and around the *s*-MRE of $r_{\text{asp}} = 17.5$. The deflected *s*-MRE under an actuation field $b_2^{\text{actu}} \approx 0.2$ T, i.e., at the last converged point on (a) is shown on (b–d).

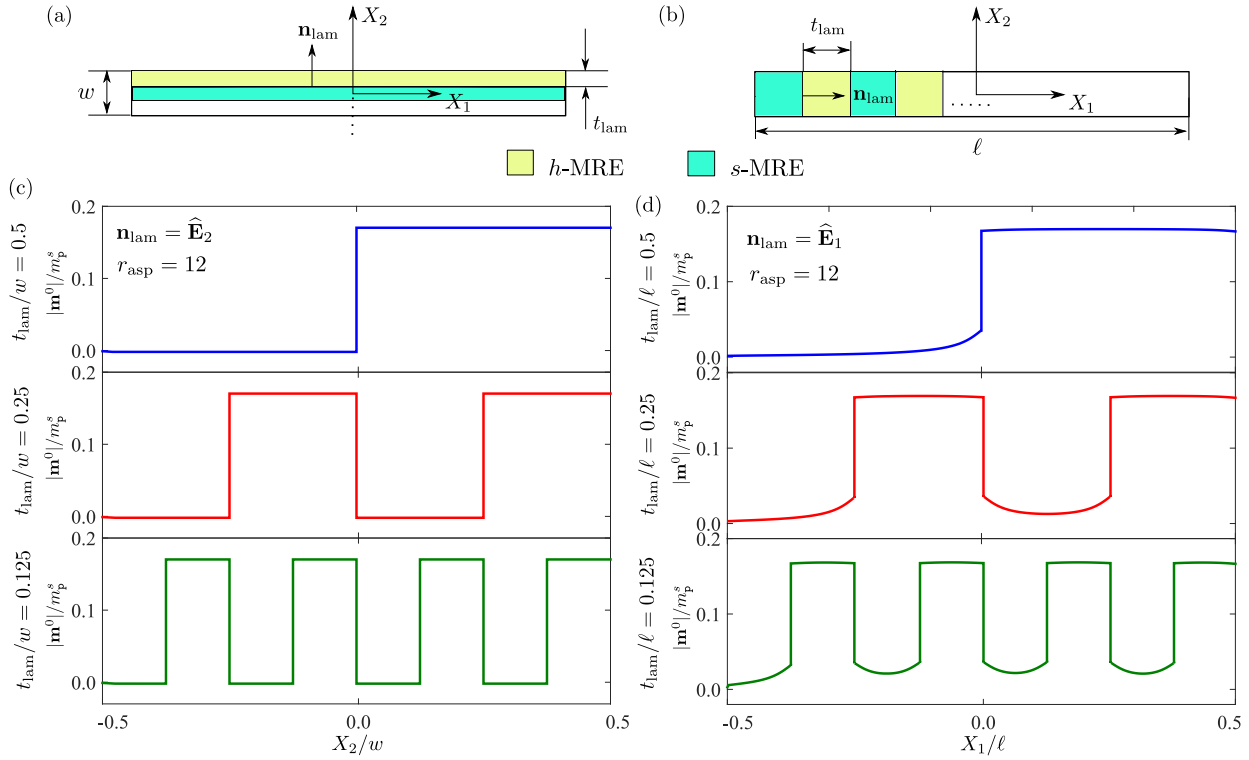

Fig. 10. Schematic diagram of rank-1 laminates comprising *h*-MRE and *s*-MRE layers with the uniform layer thickness t_{lam} and unit normal $\mathbf{n}_{\text{lam}}$ on the laminate interface along (a) $\widehat{\mathbf{E}}_2$ and (b) $\widehat{\mathbf{E}}_1$. Variation of the remanent magnetization magnitude along the centerlines of the laminates in the direction of $\mathbf{n}_{\text{lam}}$ for different t_{lam} values and for (c) $\mathbf{n}_{\text{lam}} = \widehat{\mathbf{E}}_2$ and (d) $\mathbf{n}_{\text{lam}} = \widehat{\mathbf{E}}_1$.

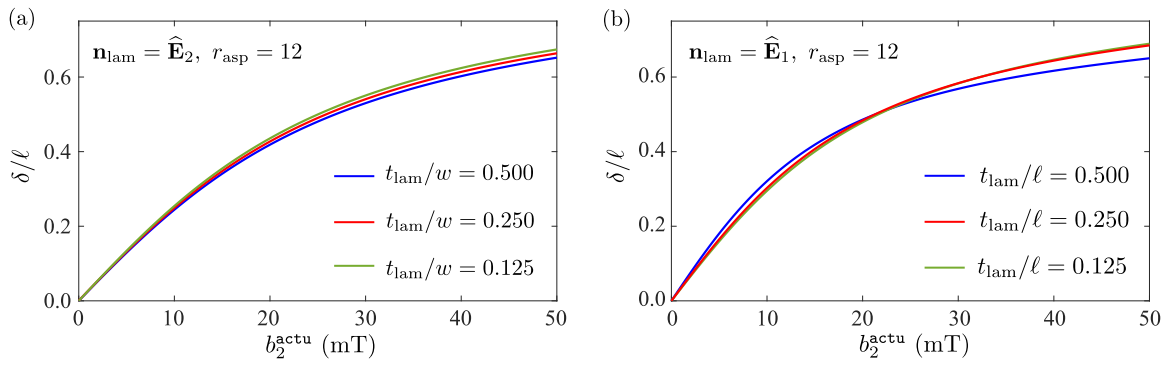

Fig. 11. End-tip deflection of the cantilevered h-/s-MRE laminates with overall $r_{\rm asp} = 12$ and (a) $\mathbf{n}_{\rm lam} = \widehat{\mathbf{E}}_2$,(b) $\mathbf{n}_{\rm lam} = \widehat{\mathbf{E}}_1$ under the actuation field $b_2^{\rm actu}$ along $\widehat{\mathbf{E}}_2$. Effect of a decreasing $t_{\rm lam}$ on the end-tip deflections are shown.

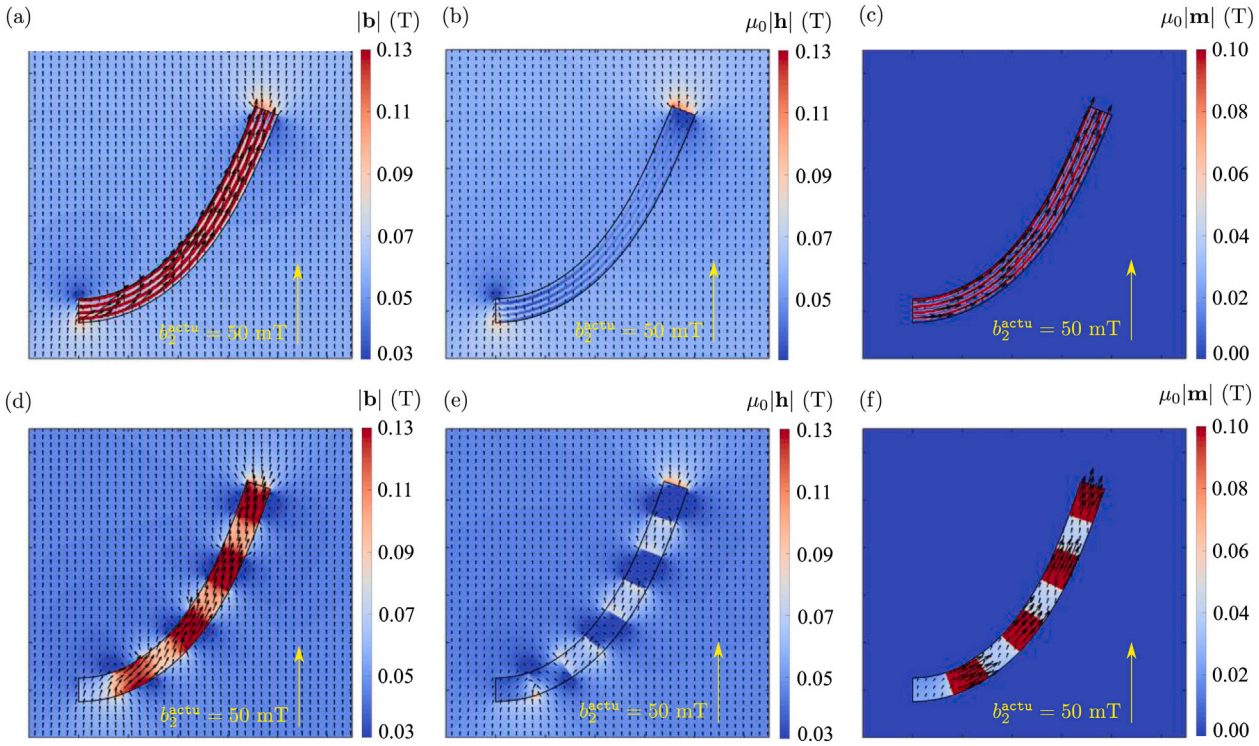

Fig. 12. Magnitude contours along with the directions of the (a, d) $\mathbf{b}$, (b, e) $\mathbf{h}$ and (c, f) $\mathbf{m}$ fields in and around the deflected cantilevered laminates of overall $r_{\rm asp} = 12$ under actuation field $b_2^{\rm actu} = 50$ mT. Two specific laminates having (a–c) $\mathbf{n}_{\rm lam} = \widehat{\mathbf{E}}_2$, $t_{\rm lam}/w = 0.125$ and (d–f) $\mathbf{n}_{\rm lam} = \widehat{\mathbf{E}}_1$, $t_{\rm lam}/\ell = 0.125$ are shown.

6.4. Non-uniformly pre-magnetized, functionally-graded h-MRE cantilever beams

The increasing trend in the development of remotely-actuated locomotion of milli-robotic structures necessitates the employment of non-uniformly pre-magnetized h-MREs, exhibiting preferential deflections patterns depending on the actuation field directions (Ren et al., 2019; Alapan et al., 2020). Motivated from these recent applications, we employ the proposed incremental variational framework in the investigation of non-uniformly pre-magnetized h-MREs, specifically towards their pre-magnetization patterns and actuation performances.

In particular, we consider a slender h-MRE beam with $r_{\rm asp} = 20$, $G_{\rm m} = 0.187$ MPa and profile it according to the configurations shown in Fig. 13a and b before applying the pre-magnetization field along $\widehat{\mathbf{E}}_2$. Depending on this pre-magnetization profiling, the h-MREs are categorized into two, namely, $\mathcal{S}_1$ and $\mathcal{S}_2$, as indicated on Fig. 13a and b. Moreover, we consider two more types of h-MREs, namely, $\mathcal{T}_1$ and $\mathcal{T}_2$, depending on the spatial distribution of the particle volume fraction. In particular, we consider a constant $c = 0.177$ for type $\mathcal{T}_1$, while a linearly varying c along the reference coordinate X_1 so that $c = 0.054 + 0.492|X_1|/\ell$ for the type $\mathcal{T}_2$ (see Fig. 13c). Notice that the *cumulative volume* of the hard-magnetic particles are considered to be identical in $\mathcal{T}_1$ and $\mathcal{T}_2$, so that the areas under both the curves in Fig. 13c remain identical. Hence, we investigate the transverse actuation response of four distinct pre-magnetized h-MREs, namely, $\mathcal{S}_i\mathcal{T}_j$, where $i, j \equiv 1, 2$.

Evidently, the initial profiling of the h-MRE beams and their release after the pre-magnetization necessitates a couple of additional steps of mechanical loading compared to the examples presented in Sections 6.1–6.3. These steps read

- `Step-I`: First, the profiling of the undeformed to the pre-magnetization shapes are performed by applying a prescribed displacement $\mathbf{u}_\tau = \mathbf{u}_\tau^{\rm Top}$ for all $\mathbf{X} \in \partial\mathcal{V}_{\rm MRE}^{\rm Top}$ for $\mathcal{S}_1$ and $\mathbf{u}_\tau = \mathbf{u}_\tau^{\rm Top}$ for all $\mathbf{X} \in \partial\mathcal{V}_{\rm MRE}^{\rm Top}$, $X_1 > 0$ and $\mathbf{u}_\tau = \mathbf{u}_\tau^{\rm Bottom}$ for all $\mathbf{X} \in \partial\mathcal{V}_{\rm MRE}^{\rm Bottom}$, $X_1 <$

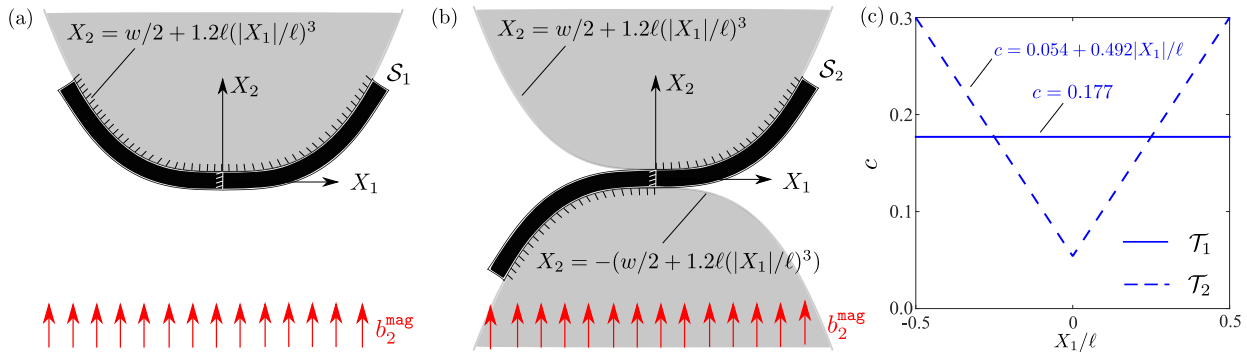

Fig. 13. (a, b) Pre-magnetization profiles along the magnetizing field b_2^{mag} direction for the h-MRE beams of $r_{\text{asp}} = 20$. The profile $\mathcal{S}_1$ in (a) is considered to be the mirror image with respect to X_2 axis, whereas, $\mathcal{S}_2$ in (b) is considered to be the mirror image with respect to both, X_1 and X_2. (c) Volume fraction distribution profiles, namely, $\mathcal{T}_1$ and $\mathcal{T}_2$, along the length of the beam.

0 for $\mathcal{S}_2$[7]. In addition, we set $\mathbf{u}_\tau = \mathbf{0}$ for all $\mathbf{X} \in \partial\mathcal{V}_{\text{Air}}$ and for all $\mathbf{X} \in \mathcal{V}_{\text{MRE}}$ if $X_1 = 0$, i.e., the displacements of the central vertical section of the beam are also blocked.

- `Step-II`: Next, the pre-magnetization is carried out along $\widehat{\mathbf{E}}_2$ in terms of applying a suitable Dirichlet boundary condition on φ_τ similar to Section 6.1. Moreover, the temporal profile and amplitude of $(b_2^{\text{mag}})_\tau$ remains identical to that of $(b_1^{\text{mag}})_\tau$ in Section 6.1.
- `Step-III`: This step gradually releases the constraints on $\mathbf{u}_\tau$ for all $\mathbf{X} \in \partial\mathcal{V}_{\text{MRE}}^{\text{Top}}$ and $\mathbf{X} \in \partial\mathcal{V}_{\text{MRE}}^{\text{Bottom}}$, while keeping $\mathbf{u}_\tau = \mathbf{0}$ at $\mathcal{V}_{\text{Air}}$ and the central vertical section of the beam. The beam comes back to its (almost) undeformed shape after this step.
- `Step-IV`: This is essentially the actuation step where the field $(b_2^{\text{actu}})_\tau$ is applied along $\widehat{\mathbf{E}}_2$. Hence, the Dirichlet boundary condition on φ_τ is set identical to (6.5), while that on $\mathbf{u}_\tau$ remain the same as at the end of `Step-III`.

The first key outcome from the aforementioned magneto-mechanical loading exercise is the variation of the remanent magnetization $\mathbf{m}^0$ along the beam's centerline at the end of `Step-III`. Specifically, the variation of the magnitude of $\mathbf{m}^0$ and its angle with $\widehat{\mathbf{E}}_1$ for all four combinations of pre-magnetization and c profiles, namely, $\mathcal{S}_i\mathcal{T}_j$ with $i, j \equiv 1, 2$ are shown in Fig. 14a and b, respectively. In agreement with the experimental observations (Ren et al., 2019; Alapan et al., 2020), the magnitude of $\mathbf{m}^0$ remains the same in the beams $\mathcal{S}_1\mathcal{T}_1$ and $\mathcal{S}_2\mathcal{T}_1$, which have a spatially uniform c. The beams $\mathcal{S}_1\mathcal{T}_2$ and $\mathcal{S}_2\mathcal{T}_2$, on the other hand, exhibit a variation of $|\mathbf{m}^0|$ along the centerline. In fact this variation is proportional to the c variation in these beams. Thus, $|\mathbf{m}^0|$ in the beam is primarily controlled by c. In contrast, the orientation of $\mathbf{m}^0$ is dictated by its pre-magnetization profile $\mathcal{S}_1$ and $\mathcal{S}_2$ (see Fig. 14b). While the $\mathcal{S}_1$-type beams show opposite $\mathbf{m}^0$ directions along its two flanks, the direction of $\mathbf{m}^0$ in $\mathcal{S}_2$-type beams are identical in both the flanks, hence, showing a *bell curve* like variation in angle with the X_1 axis. Even though $|\mathbf{m}^0|$ in the beam is predictable in terms of c, the functional relationship of the θ^{m} profiles in Fig. 14b with the respective pre-deformed shapes in Fig. 13a and b are not straightforward and cannot be predicted beforehand prior solving the full field BVP.

To obtain more insight on the complexity of the non-uniform remanent fields, we plot the spatial profiles of $\mathbf{b}^0$, $\mathbf{h}^0$ and $\mathbf{m}^0$ fields, both, in terms of magnitude and directions, in Fig. 15 for all four aforementioned types of beams. The first, and obvious feature observed is the higher magnitude of $\mathbf{b}^0$, $\mathbf{h}^0$ and $\mathbf{m}^0$ in the beams of type $\mathcal{T}_2$, which can directly be attributed to the higher c value in $\mathcal{T}_2$ near the beam flanks (cf. e.g., Figs. 15a–c and g–i). Moreover, comparing Fig. 15b, e with h, k we observe that by linearly increasing c along the flanks, the concentration of $\mathbf{h}^0$ field near the center of the beam can be eliminated. Of course, the spatial gradient of c in the $\mathcal{T}_2$-type beams results in a stiffer gradient in the $|\mathbf{b}|^0$ along the beams's centerline (cf. Figs. 15a, d and g, j).

In contrast, the directions of $\mathbf{b}^0$, $\mathbf{h}^0$ and $\mathbf{m}^0$ fields in the h-MRE along with the stray fields around the MRE domain depend strongly on their pre-magnetization profiles. Thus, we observe*qualitatively similar* stray $\mathbf{b}$ and $\mathbf{h}$ field distributions around the in all the $\mathcal{S}_1$ or $\mathcal{S}_2$-type beams, irrespective of the c distributions in them. Specifically, we observe from Figs. 15a and g that the beams with pre-magnetization profile $\mathcal{S}_1$ exhibit stronger self fields at the vicinity of their bottom boundary as compared to the top. Such preferential self-field distributions are typically achieved by constructing *Halbach chains* (Halbach, 1980; Hilton and McMurry, 2012; Mansson, 2014), which consists of an array of permanent magnets arranged in a particular fashion in order to concentrate the resulting magnetic self field at one side of the chain. A similar feature is observed here for the $\mathcal{S}_1$-type non-uniformly pre-magnetized hMRE in Figures Fig. 15a and g. Thus, a properly pre-magnetized, *monolithic* h-MRE can mimic the properties of classical, essentially heterogeneous, Halbach chain structures.

In turn, such a concentration of the magnetic self fields are not observed in the beams having the pre-magnetization profile as $\mathcal{S}_2$. Rather, the contours of higher magnetic self fields render an inverted "S"-type shapes in all the $\mathcal{S}_2$-type beams. Thus, proper profiling of the beam before the pre-magnetization may help engineering different self field distributions in the vicinity of a h-MRE. The implications of such self field distributions on the actuation response of the $\mathcal{S}_1$ and $\mathcal{S}_2$-type beams will be discussed next.

Remark 5. The $\mathbf{b}$, $\mathbf{h}$ and $\mathbf{m}$ field magnitude contours and directions in Fig. 15 reveal that the local remanent $\mathbf{b}$ and $\mathbf{m}$ fields in the h-MREs *are not* related by the relation $\mathbf{b} = \mu_0\mathbf{m}$. Hence, unlike the uniformly pre-magnetized h-MREs, it may reveal inaccurate to assume, in general, that the magnetic torque at a point in the h-MRE is simply given by $\mathbf{b}^{\text{actu}} \times \mu_0\mathbf{m}$ during the actuation under remotely applied $\mathbf{b}^{\text{actu}}$ field. Thus, even though the magnetic toque-based, reduced-order models for slender h-MRE beams exhibit sufficiently accurate deflection profiles (Wang et al., 2020; Yan et al., 2021a,b), their employment to the

[7] In practice, we employ the "DISP" subroutine of ABAQUS, which apply an user-defined displacement in terms of the *current coordinates*. We thus define the displacements $u_1^{\text{Top}} = -0.6\ell(x_1/\ell)^3$ and $u_2^{\text{Top}} = 1.2\ell(|x_1|/\ell)^3$ for $\mathcal{S}_1$ and additionally, $u_1^{\text{Bottom}} = -0.6\ell(x_1/\ell)^3$ and $u_2^{\text{Bottom}} = -1.2\ell(x_1/\ell)^3$ to achieve the deformation profile $\mathcal{S}_2$. These displacements are applied incrementally, held to the prescribed constant values and then released incrementally during the appropriate steps.

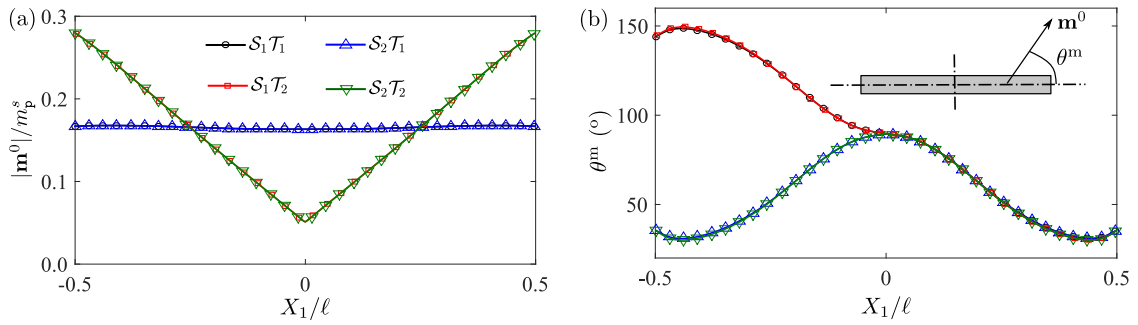

Fig. 14. Variation of the remanent magnetization $\mathbf{m}^0$ (a) magnitudes and (b) directions along the length of the pre-magnetized h-MRE beams of type $\mathcal{S}_i\mathcal{T}_i$ $(i = 1, 2)$.

non-uniformly pre-magnetized h-MRE structures must be carried out with caution and certainly use the local non-uniform pre-magnetization profile. Moreover, the pre-magnetization directions along the beam length do not exhibit any straightforward correlation with its pre-deformation geometry. Hence, solving for the full-field BVP with a surrounding air becomes inevitable even for a reduced-order analysis in the later stage.

Finally, we show the transverse magnetic actuation performance of the four types of beams, namely, $\mathcal{S}_i\mathcal{T}_j$ with $i, j \equiv 1, 2$. First, we investigate the uniformly distributed c cases, i.e., the response of $\mathcal{T}_1$-type h-MREs in Fig. 16a–c. Specifically, Figs. 16a and b show the deflected beam centerline under an actuation field $b_2^{\mathtt{actu}} = 20$ mT along $\hat{\mathbf{E}}_2$ and $-\hat{\mathbf{E}}_2$ directions. Identical deflection of both the beam flanks are observed for the beam $\mathcal{S}_1\mathcal{T}_1$. However, the deflection is substantially higher (∼2.5 times) when the fields are applied along $-\hat{\mathbf{E}}_2$. This observation can directly be attributed to the pre-magnetization direction in both the beam flanks, which, eventually leads to a higher deflection when deflecting in the opposite direction of $\mathbf{m}^0$. This preferential deflection phenomena can be termed as the *magneto-mechanical Halbach effect*. In fact, this preferential deflection property is harnessed effectively in locomotion of soft jellyfish-like swimming robot (Ren et al., 2019; Alapan et al., 2020).

Even though equal in their magnitudes, the two flanks of the $\mathcal{S}_2$-type pre-magnetized beams always deflect in the opposite direction. For example, the deflected centerline of the h-MRE beam under $b_2^{\mathtt{actu}} = 20$ mT along $\hat{\mathbf{E}}_2$ and $-\hat{\mathbf{E}}_2$ are shown in Fig. 16b. Of course, here the deflection magnitude remains identical to the $\mathcal{S}_1$-type h-MRE, but overall, leading to a rocking-type motion, where the two flanks deflect simultaneously in the opposite directions. In particular, the variation of the vertical displacement of top-right and bottom-left corners of the $\mathcal{S}_1\mathcal{T}_1$ and $\mathcal{S}_2\mathcal{T}_1$-type h-MRE beams under $b_2^{\mathtt{actu}}$ are shown in Fig. 16c. This figure clearly shows that the deflection magnitude under the same $|b_2^{\mathtt{actu}}|$ becomes ∼ 2.5 times when the direction of its application is along $-\hat{\mathbf{E}}_2$.

The $\mathcal{T}_2$-type beams exhibit a qualitatively similar deflection response under $b_2^{\mathtt{actu}}$ *vis-a-vis* the $\mathcal{T}_1$-type. The only and obvious difference between the former and the latter is that the $\mathcal{T}_2$-type beams deflect the same amount at a lower actuation field (∼0.75 times). The deflected shapes of the $\mathcal{S}_1\mathcal{T}_2$ and $\mathcal{S}_2\mathcal{T}_2$-type beams are shown in Figs. 16d and e, respectively, both, under $b_2^{\mathtt{actu}} = 12.5$ and -12.5. Finally, the deflection variation of the top-right and bottom-left corners of, respectively, $\mathcal{S}_1\mathcal{T}_2$ and $\mathcal{S}_2\mathcal{T}_2$-type beams under $b_2^{\mathtt{actu}}$ are shown in Fig. 16f.

In closing, we remark that except lowering of the actuation field magnitude, the functionally-graded h-MREs with a linearly increasing c towards the beam flanks do not exhibit any substantial difference with the actuation performance of its uniform c counterpart. In turn, fabricating the functionally-graded h-MREs adds on to the difficulty level and cost. The pre-magnetization profiling, in contrast, can dramatically change the actuation performance of the h-MRE beams. In this regard, the proposed model serves as an efficient tool to analyze the effect of different pre-magnetization profiles and directions even before the manufacturing of an actual sample is carried out.

7. Concluding remarks

In this work, we propose fully-coupled, dual, continuum models for the magneto-active particle-filled isotropic, incompressible (and *quasi-incompressible*) MREs in the $\mathbf{F}-\mathbf{H}$ and $\mathbf{F}-\mathbf{B}$ variable spaces. Both models are fully explicit and have direct dependence on the mechanical and magnetic properties pf the MRE's constituents, i.e., the elastomer matrix and magneto-active particles, along with the particle volume fraction. The only scalar phenomenological parameter introduced in the models is a coupling parameter that depends solely on the particle volume fraction and is calibrated from full-field numerical homogenization estimates.

Specifically, we first frame a fully Lagrangian, rate-type variational framework for the scalar potential-based $\mathbf{F}-\mathbf{H}$ modeling of dissipative h-MREs, where we introduce a thermodynamic internal variable $\boldsymbol{\xi}$. This variable resembles closely the (local) remanent magnetization in the material. The vector potential-based $\mathbf{F}-\mathbf{B}$ variational framework is defined simultaneously by expressing the magnetic energy density W^{B} in terms of the partial Legendre–Fenchel transform with respect to $\mathbf{H}$ of its $\mathbf{F}-\mathbf{H}$-based counterpart W^{H}. By construction, the $\mathbf{F}-\mathbf{B}$ model involves the same internal variable $\boldsymbol{\xi}$. Moreover, the dissipation potential D, expressed only in terms of $|\dot{\boldsymbol{\xi}}|$, remains the same in both the models.

Specific functional forms for the energetic W^{H} and dissipation D potentials are then introduced following the recent $\mathbf{F}-\mathbf{H}$-based h-MRE model of Mukherjee et al. (2021). Being strictly concave in terms of $\mathbf{H}$, the $\mathbf{F}-\mathbf{H}$ energy density W^{H} admits a closed form partial Legendre–Fenchel transform with respect to $\mathbf{H}$, eventually leading to an explicit W^{B}, i.e., the $\mathbf{F}-\mathbf{B}$-based energy density. Consequently, we have the exact $\mathbf{F}-\mathbf{B}$ equivalent of the $\mathbf{F}-\mathbf{H}$-based model, involving the same particle, matrix and coupling parameters. Thus, starting from the equivalent $\mathbf{F}-\mathbf{H}$ and $\mathbf{F}-\mathbf{B}$-based variational principles, we have stated the explicit forms of the energy density functions, which can be independently employed to calculate the model response and solve various BVPs.

The important limiting case of vanishing particle coercivity $b_{\mathrm{p}}^c \to 0$ leads to a seamless class of dual s-MRE models, which exhibits a reversible, purely energetic magneto-mechanical response. Of course, in this limit, the dissipation potential $\mathscr{D}$ vanishes and $\boldsymbol{\xi}$ is given in terms of $\mathbb{C}$ and $\mathbf{H}$ or $\mathbf{B}$ depending on the independent variable we choose. Thus, the proposed h-MRE models are simply general models for any type of MREs since the h- and s-MRE model response can be obtained from the exact same model by simply setting $0 < b_{\mathrm{p}}^c \ll 1$ for the latter. Furthermore, the expression(s) for the total Cauchy stress $\boldsymbol{\sigma}$ in $\mathbf{F}-\mathbf{H}$ and $\mathbf{F}-\mathbf{B}$ models in the $b_{\mathrm{p}}^c \to 0$ limit become identical to those obtained by Kankanala and Triantafyllidis (2004), Dorfmann and Ogden (2004) for the specific case of s-MREs. In this sense, this paper provides a

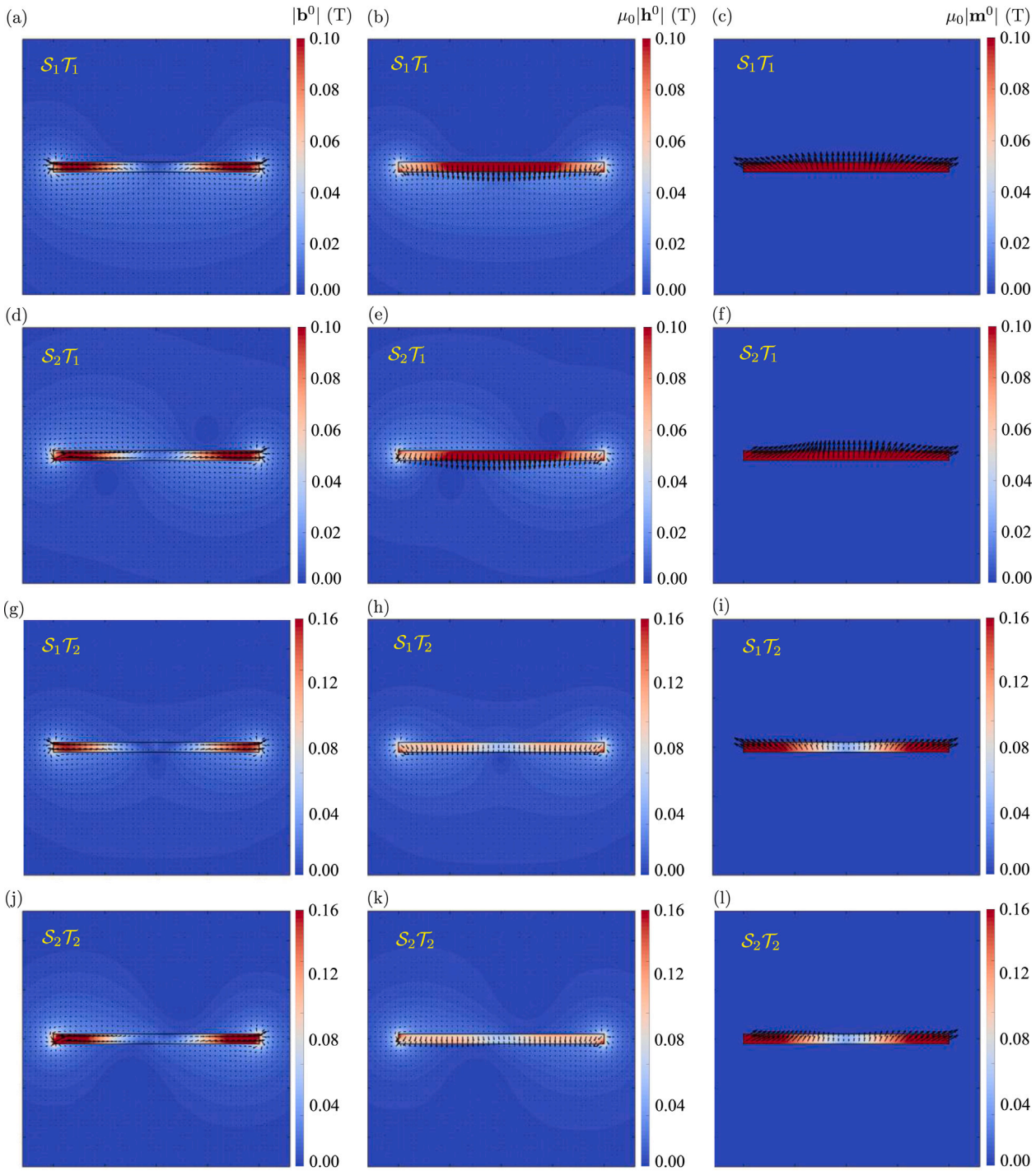

Fig. 15. Magnitude contours along with the directions of the remanent $\mathbf{b}^0$, $\mathbf{h}^0$ and $\mathbf{m}^0$ fields *after* the pre-magnetization step (Step-3) for the *h*-MRE types (depending on the pre-deformation profile and particle distribution) (a–c) $\mathcal{S}_1\mathcal{T}_1$, (d–f) $\mathcal{S}_2\mathcal{T}_1$, (g–i) $\mathcal{S}_1\mathcal{T}_2$ and (j–l) $\mathcal{S}_2\mathcal{T}_2$.

unified approach towards a *microstructurally-guided* modeling of MREs, both, in the $\mathbf{F}-\mathbf{H}$ and $\mathbf{F}-\mathbf{B}$ variable spaces.

Numerical solution of the fully coupled magneto-mechanical BVPs necessitates further specialization of the rate-type variational formulations in a time-discrete form. Moreover, following Rosato and Miehe (2014), we introduce the notion of a *reduced potential* that facilitates the finite-element solution for the dissipative materials by locally updating the internal variables *prior* to solving the global BVP. The predictive capabilities of the proposed models for the deflection of pre-magnetized slender *h*-MREs are probed against the experimental measurements of Zhao et al. (2019). Besides predicting the deflection of the uniformly pre-magnetized *h*-MREs, the model is employed to investigate the magnetic actuation performance of a number of slender MRE structures having non-uniform remanent magnetization fields. In particular, the magnetic actuation response of the rank-1 *h*-/*s*-MRE laminates and non-uniformly pre-magnetized, functionally-graded *h*-MREs are shown in Section 6. The intricate remanent **b**, **h** and **m** fields in the MRE observed for the latter cases are impossible to predict beforehand. Thus, employing the fully coupled, dissipative frameworks becomes unavoidable before analyzing any magneto-active structure beyond the uniformly pre-magnetized slender beams.

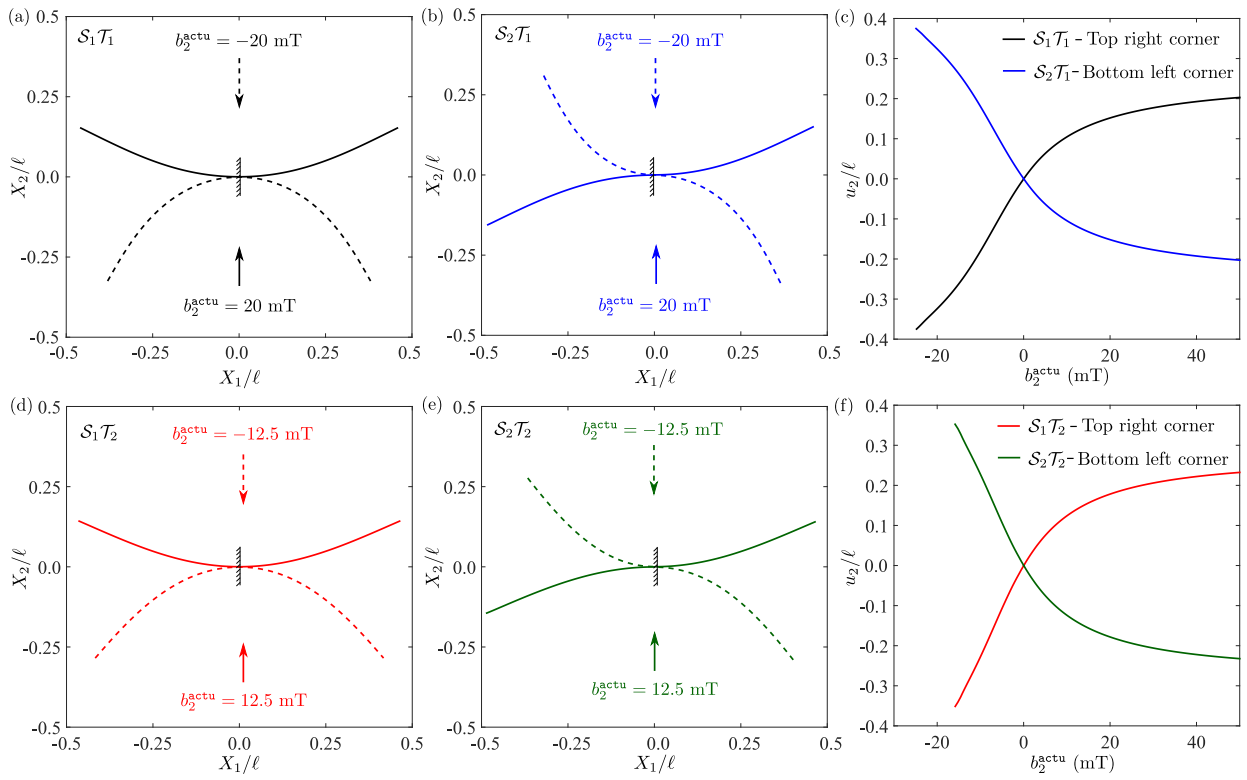

Fig. 16. Deflected centerlines of the h-MREs type (a) $\mathcal{S}_1\mathcal{T}_1$ and (b) $\mathcal{S}_2\mathcal{T}_1$ under the actuation fields $b_2^{\text{actu}} = 20$ and -20 mT along $\hat{\mathbf{E}}_2$. (c) Variation of the top-right corner delfection of $\mathcal{S}_1\mathcal{T}_1$ and bottom left corner delfection $\mathcal{S}_2\mathcal{T}_1$ under b_2^{actu}. Deflected centerlines of the h-MREs type (d) $\mathcal{S}_1\mathcal{T}_2$ and (e) $\mathcal{S}_2\mathcal{T}_2$ under the actuation fields $b_2^{\text{actu}} = 12.5$ and -12.5 mT along $\hat{\mathbf{E}}_2$. (f) Variation of the top-right corner delfection of $\mathcal{S}_1\mathcal{T}_2$ and bottom left corner delfection $\mathcal{S}_2\mathcal{T}_2$ under b_2^{actu}.

Efficient modeling of the surrounding air domain is necessary to accommodate large deflections of the MREs and the interactions between two pre-magnetized MREs through air. Although the air node constraining method used here performs a fairly decent jobs in modeling large deflection of the MRE beams, this approach becomes cumbersome when modeling complicated structures with intricate geometries. Thus, there exists ample scope of improving the numerical modeling of surrounding air. Perhaps, a mesh-free Lagrangian finite element method in the lines of Kumar et al. (2019) would be useful to overcome the aforementioned shortcomings.

In closing, we remark that, even though most of the experimental works and the examples chosen in this paper concern different actuation performance of the uniformly and non-uniformly pre-magnetized MREs, there exist a vast opportunity of engineering the magnetic self fields around a structure by optimizing the spatial distribution of the particle volume fraction and the pre-deformation of the MRE. In this regard, we observe a number of attempts of stray magnetic field engineering using the metallic hard magnets (Lee et al., 2017; Kee et al., 2020). However, achieving the same using a *monolithic and flexible* MRE structure still remains unaddressed.

Declaration of competing interest

The authors declare that they have no known competing financial interests or personal relationships that could have appeared to influence the work reported in this paper.

Acknowledgments

The authors would like to acknowledge support from the European Research Council (ERC) under the European Union's Horizon 2020 research and innovation program (grant agreement No. 636903 - MAGNETO). The computational part of this work was also supported by the ANR, France under contract number ANR-10-EQPX-37. The Abaqus user defined element (UEL) developed for the numerical simulations using the proposed **F**−**H** model along with a representative example are available at https://www.doi.org/10.5281/zenodo.4588578. The **F** − **B** model UEL will be made available upon request.

References

Abbott, J.J., Ergeneman, O., Kummer, M.P., Hirt, A.M., Nelson, B.J., 2007. Modeling magnetic torque and force for controlled manipulation of soft-magnetic bodies. IEEE Trans. Robot. 23, 1247–1252. http://dx.doi.org/10.1109/TRO.2007.910775.

Alapan, Y., Karacakol, A.C., Guzelhan, S.N., Isik, I., Sitti, M., 2020. Reprogrammable shape morphing of magnetic soft machines. Sci. Adv. 6, eabc6414. http://dx.doi.org/10.1126/sciadv.abc6414.

Bassiouny, E., Ghaleb, A., Maugin, G., 1988. Thermodynamical formulation for coupled electromechanical hysteresis effects– I. Basic equations. Internat. J. Engrg. Sci. 26, 1279–1295. http://dx.doi.org/10.1016/0020-7225(88)90047-x.

Bastola, A.K., Hossain, M., 2021. The shape – morphing performance of magnetoactive soft materials. Mater. Des. 211, 110172. http://dx.doi.org/10.1016/j.matdes.2021.110172.

Bira, N., Dhagat, P., Davidson, J.R., 2020. A review of magnetic elastomers and their role in soft robotics. Front. Robot. AI 7, http://dx.doi.org/10.3389/frobt.2020.588391.

Biro, O., Preis, K., 1989. On the use of the magnetic vector potential in the finite-element analysis of three-dimensional eddy currents. IEEE Trans. Magn. 25, 3145–3159. http://dx.doi.org/10.1109/20.34388.

Bodelot, L., Voropaieff, J.P., Pössinger, T., 2017. Experimental investigation of the coupled magneto-mechanical response in magnetorheological elastomers. Exp. Mech. 58, 207–221. http://dx.doi.org/10.1007/s11340-017-0334-7.

Brown, W.F., 1966. Magnetoelastic Interactions, Vol. 9. Springer.

Bustamante, R., Dorfmann, A., Ogden, R., 2008. On variational formulations in nonlinear magnetoelastostatics. Math. Mech. Solids 13, 725–745. http://dx.doi.org/10.1177/1081286507079832.

Chen, Y.C., Wheeler, L., 1993. Derivatives of the stretch and rotation tensors. J. Elasticity 32, 175–182. http://dx.doi.org/10.1007/bf00131659.

Danas, K., 2017. Effective response of classical, auxetic and chiral magnetoelastic materials by use of a new variational principle. J. Mech. Phys. Solids 105, 25–53. http://dx.doi.org/10.1016/j.jmps.2017.04.016.

Danas, K., Kankanala, S., Triantafyllidis, N., 2012. Experiments and modeling of iron-particle-filled magnetorheological elastomers. J. Mech. Phys. Solids 60, 120–138. http://dx.doi.org/10.1016/j.jmps.2011.09.006, http://www.sciencedirect.com/science/article/pii/S0022509611001736.

Danas, K., Triantafyllidis, N., 2014. Instability of a magnetoelastic layer resting on a non-magnetic substrate. J. Mech. Phys. Solids 69, 67–83. http://dx.doi.org/10.1016/j.jmps.2014.04.003.

Dorfmann, A., Ogden, R., 2003. Magnetoelastic modelling of elastomers. Eur. J. Mech. A Solids 22, 497–507. http://dx.doi.org/10.1016/s0997-7538(03)00067-6.

Dorfmann, A., Ogden, R., 2004. Nonlinear magnetoelastic deformations of elastomers. Acta Mech. 167, 13–28. http://dx.doi.org/10.1007/s00707-003-0061-2.

Dorfmann, A., Ogden, R., 2005. Some problems in nonlinear magnetoelasticity. Zeitschrift FÜr AngewandTe Mathematik Und Physik ZAMP 56, 718–745. http://dx.doi.org/10.1007/s00033-004-4066-z.

Dorn, C., Bodelot, L., Danas, K., 2021. Experiments and numerical implementation of a boundary value problem involving a magnetorheological elastomer layer subjected to a nonuniform magnetic field. J. Appl. Mech. 88, http://dx.doi.org/10.1115/1.4050534.

Ethiraj, G., Miehe, C., 2016. Multiplicative magneto-elasticity of magnetosensitive polymers incorporating micromechanically-based network kernels. Internat. J. Engrg. Sci. 102, 93–119. http://dx.doi.org/10.1016/j.ijengsci.2015.08.007.

Galipeau, E., Ponte Castañda, P., 2013. A finite-strain constitutive model for magnetorheological elastomers: Magnetic torques and fiber rotations. J. Mech. Phys. Solids 61, 1065–1090. http://dx.doi.org/10.1016/j.jmps.2012.11.007.

Garcia-Gonzalez, D., 2019. Magneto-visco-hyperelasticity for hard-magnetic soft materials: theory and numerical applications. Smart Mater. Struct. 28, 085020. http://dx.doi.org/10.1088/1361-665x/ab2b05.

Garcia-Gonzalez, D., Hossain, M., 2020. A microstructural-based approach to model magneto-viscoelastic materials at finite strains. Int. J. Solids Struct. http://dx.doi.org/10.1016/j.ijsolstr.2020.10.028, http://www.sciencedirect.com/science/article/pii/S0020768320304224.

Gerbal, F., Wang, Y., Lyonnet, F., Bacri, J.C., Hocquet, T., Devaud, M., 2015. A refined theory of magnetoelastic buckling matches experiments with ferromagnetic and superparamagnetic rods. Proc. Natl. Acad. Sci. 112, 7135–7140. http://dx.doi.org/10.1073/pnas.1422534112, http://www.pnas.org/content/112/23/7135.abstract, http://arxiv.org/abs/http://www.pnas.org/content/112/23/7135.full.pdf.

Halbach, K., 1980. Design of permanent multipole magnets with oriented rare earth cobalt material. Nucl. Instrum. Methods 169, 1–10. http://dx.doi.org/10.1016/0029-554x(80)90094-4.

Halphen, B., Son Nguyen, Q., 1975. Sur les matériaux standard généralisés. Journal de MÉcanique 14, 39–63.

Hilton, J., McMurry, S., 2012. An adjustable linear halbach array. J. Magn. Magn. Mater. 324, 2051–2056. http://dx.doi.org/10.1016/j.jmmm.2012.02.014, https://www.sciencedirect.com/science/article/pii/S030488531200100X.

Huber, J.E., Fleck, N.A., 2001. Multi-axial electrical switching of a ferroelectric: theory versus experiment. J. Mech. Phys. Solids 49, 785–811. http://dx.doi.org/10.1016/s0022-5096(00)00052-1.

Huber, J.E., Fleck, N.A., Landis, C.M., McMeeking, R.M., 1999. A constitutive model for ferroelectric polycrystals. J. Mech. Phys. Solids 47, 1663–1697. http://dx.doi.org/10.1016/s0022-5096(98)00122-7.

Idiart, M., Moulinec, H., Castañeda, P.P., Suquet, P., 2006. Macroscopic behavior and field fluctuations in viscoplastic composites: second-order estimates versus full-field simulations. J. Mech. Phys. Solids 54, 1029–1063. http://dx.doi.org/10.1016/j.jmps.2005.11.004, http://www.sciencedirect.com/science/article/pii/S0022509605002188.

Javili, A., Chatzigeorgiou, G., Steinmann, P., 2013. Computational homogenization in magneto-mechanics. Int. J. Solids Struct. 50, 4197–4216. http://dx.doi.org/10.1016/j.ijsolstr.2013.08.024.

Kalina, K.A., Brummund, J., Metsch, P., Kästner, D.Y., Linke, J.M., Odenbach, S., 2017. Modeling of magnetic hystereses in soft mres filled with ndfeb particles. Smart Mater. Struct. 26, 105019. http://dx.doi.org/10.1088/1361-665x/aa7f81.

Kankanala, S., Triantafyllidis, N., 2004. On finitely strained magnetorheological elastomers. J. Mech. Phys. Solids 52, 2869–2908. http://dx.doi.org/10.1016/j.jmps.2004.04.007.

Kee, H., Lee, H., Park, S., 2020. Optimized halbach array for focused magnetic drug targeting. J. Magn. Magn. Mater. 514, 167180. http://dx.doi.org/10.1016/j.jmmm.2020.167180.

Keip, M.A., Rambausek, M., 2016. A multiscale approach to the computational characterization of magnetorheological elastomers. Internat. J. Numer. Methods Engrg. 107, 338–360. http://dx.doi.org/10.1002/nme.5178.

Keip, M.A., Rambausek, M., 2017. Computational and analytical investigations of shape effects in the experimental characterization of magnetorheological elastomers. Int. J. Solids Struct. 121, 1–20. http://dx.doi.org/10.1016/j.ijsolstr.2017.04.012.

Kim, Y., Yuk, H., Zhao, R., Chester, S.A., Zhao, X., 2018. Printing ferromagnetic domains for untethered fast-transforming soft materials. Nature 558, 274–279. http://dx.doi.org/10.1038/s41586-018-0185-0.

Klinkel, S., 2006. A phenomenological constitutive model for ferroelastic and ferroelectric hysteresis effects in ferroelectric ceramics. Int. J. Solids Struct. 43, 7197–7222. http://dx.doi.org/10.1016/j.ijsolstr.2006.03.008.

Kumar, S., Danas, K., Kochmann, D.M., 2019. Enhanced local maximum-entropy approximation for stable meshfree simulations. Comput. Methods Appl. Mech. Engrg. 344, 858–886. http://dx.doi.org/10.1016/j.cma.2018.10.030.

Landis, C.M., 2002. Fully coupled, multi-axial, symmetric constitutive laws for polycrystalline ferroelectric ceramics. J. Mech. Phys. Solids 50, 127–152. http://dx.doi.org/10.1016/s0022-5096(01)00021-7.

Lee, J., Nomura, T., Dede, E.M., 2017. Topology optimization of halbach magnet arrays using isoparametric projection. J. Magn. Magn. Mater. 432, 140–153. http://dx.doi.org/10.1016/j.jmmm.2017.01.092.

Lefère, K., Lopez-Pamies, O., 2017. A general result for the magnetoelastic response of isotropic suspensions of iron and ferrofluid particles in rubber, with applications to spherical and cylindrical specimens. J. Mech. Phys. Solids 107, 343–364. http://dx.doi.org/10.1016/j.jmps.2017.06.017.

Lefèvre, K., Lopez-Pamies, O., 2020. Two families of explicit models constructed from a homogenization solution for the magnetoelastic response of MREs containing iron and ferrofluid particles. Int. J. Non-Linear Mech. 119, 103362. http://dx.doi.org/10.1016/j.ijnonlinmec.2019.103362, http://www.sciencedirect.com/science/article/pii/S0020746219306237.

Linke, J.M., Borin, D.Y., Odenbach, S., 2016. First-order reversal curve analysis of magnetoactive elastomers. RSC Adv. 6, 100407–100416. http://dx.doi.org/10.1039/c6ra23435f.

Linnemann, K., Klinkel, S., Wagner, W., 2009. A constitutive model for magnetostrictive and piezoelectric materials. Int. J. Solids Struct. 46, 1149–1166. http://dx.doi.org/10.1016/j.ijsolstr.2008.10.014.

Lopez-Pamies, O., Goudarzi, T., Danas, K., 2013. The nonlinear elastic response of suspensions of rigid inclusions in rubber: Ii–a simple explicit approximation for finite-concentration suspensions. J. Mech. Phys. Solids 61, 19–37. http://dx.doi.org/10.1016/j.jmps.2012.08.013.

Lucarini, S., Hossain, M., Garcia-Gonzalez, D., 2022. Recent advances in hard-magnetic soft composites: Synthesis, characterisation, computational modelling, and applications. Compos. Struct. 279, 114800. http://dx.doi.org/10.1016/j.compstruct.2021.114800.

Lum, G., Ye, Z., Dong, X., Marvi, H., Erin, O., Hu, W., Sitti, M., 2016. Shape-programmable magnetic soft matter. PNAS Proc. Natl. Acad. Sci. 113, E6007–E6015.

Mansson, D., 2014. On the suitability of using halbach arrays as potential energy storage media. Prog. Electromagn. Res. B 58, 151–166. http://dx.doi.org/10.2528/pierb14010704.

Miehe, C., Rosato, D., Kiefer, B., 2011. Variational principles in dissipative electro-magneto-mechanics: A framework for the macro-modeling of functional materials. Internat. J. Numer. Methods Engrg. 86, 1225–1276. http://dx.doi.org/10.1002/nme.3127.

Mukherjee, D., 2020. Theoretical and Numerical Modeling of Magnetorheological Elastomers Comprising Magnetically Soft and Hard Particles. (Ph.D. thesis).

Mukherjee, D., Bodelot, L., Danas, K., 2020. Microstructurally-guided explicit continuum models for isotropic magnetorheological elastomers with iron particles. Int. J. Non-Linear Mech. 103380. http://dx.doi.org/10.1016/j.ijnonlinmec.2019.103380.

Mukherjee, D., Danas, K., 2019. An evolving switching surface model for ferromagnetic hysteresis. J. Appl. Phys. 125, 033902. http://dx.doi.org/10.1063/1.5051483.

Mukherjee, D., Rambausek, M., Danas, K., 2021. An explicit dissipative model for isotropic hard magnetorheological elastomers. J. Mech. Phys. Solids 151, 104361. http://dx.doi.org/10.1016/j.jmps.2021.104361.

Onsager, L., 1931a. Reciprocal relations in irreversible processes. I. Phys. Rev. 37, 405–426. http://dx.doi.org/10.1103/physrev.37.405.

Onsager, L., 1931b. Reciprocal relations in irreversible processes. II. Phys. Rev. 38, 2265–2279. http://dx.doi.org/10.1103/physrev.38.2265.

Pao, Y.H., Hutter, K., 1975. Electrodynamics for moving elastic solids and viscous fluids. Proc. IEEE.

Petrosyan, R., 2016. Improved approximations for some polymer extension models. Rheol. Acta 56, 21–26. http://dx.doi.org/10.1007/s00397-016-0977-9.

Polukhov, E., Keip, M.A., 2021. Multiscale stability analysis of periodic magnetorheological elastomers. Mech. Mater. 159, 103699. http://dx.doi.org/10.1016/j.mechmat.2020.103699.

Ponte Castañda, P., Galipeau, E., 2011. Homogenization-based constitutive models for magnetorheological elastomers at finite strain. J. Mech. Phys. Solids 59, 194–215. http://dx.doi.org/10.1016/j.jmps.2010.11.004.

Psarra, E., Bodelot, L., Danas, K., 2017. Two-field surface pattern control via marginally stable magnetorheological elastomers. Soft Matter 13, 6576–6584. http://dx.doi.org/10.1039/c7sm00996h.

Psarra, E., Bodelot, L., Danas, K., 2019. Wrinkling to crinkling transitions and curvature localization in a magnetoelastic film bonded to a non-magnetic substrate. J. Mech. Phys. Solids 133, 103734. http://dx.doi.org/10.1016/j.jmps.2019.103734.

Rambausek, M., Danas, K., 2021. Bifurcation of magnetorheological film– substrate elastomers subjected to biaxial pre-compression and transverse magnetic fields. Int. J. Non-Linear Mech. 128, 103608. http://dx.doi.org/10.1016/j.ijnonlinmec.2020.103608.

Rambausek, M., Keip, M.A., 2018. Analytical estimation of non-local deformation-mediated magneto-electric coupling in soft composites. Proc. R. Soc. Lond. Ser. A Math. Phys. Eng. Sci. 474, 20170803. http://dx.doi.org/10.1098/rspa.2017.0803, http://rspa.royalsocietypublishing.org/content/474/2216/20170803.

Rambausek, M., Mukherjee, D., Danas, K., 2022. A computational framework for magnetically hard and soft viscoelastic magnetorheological elastomers. Comp. Meth. App. Mech. Eng. 391, 114500. http://dx.doi.org/10.1016/j.cma.2021.114500.

Ren, Z., Hu, W., Dong, X., Sitti, M., 2019. Multi-functional soft-bodied jellyfish-like swimming. Nature Commun. 10, http://dx.doi.org/10.1038/s41467-019-10549-7.

Rosato, D., Miehe, C., 2014. Dissipative ferroelectricity at finite strains. variational principles, constitutive assumptions and algorithms. Internat. J. Engrg. Sci. 74, 162–189. http://dx.doi.org/10.1016/j.ijengsci.2013.08.007.

Stark, S., Semenov, A.S., Balke, H., 2015. On the boundary conditions for the vector potential formulation in electrostatics. Internat. J. Numer. Methods Engrg. 102, 1704–1732. http://dx.doi.org/10.1002/nme.4859.

Wang, L., Kim, Y., Guo, C.F., Zhao, X., 2020. Hard-magnetic elastica. J. Mech. Phys. Solids 142, 104045. http://dx.doi.org/10.1016/j.jmps.2020.104045.

Wang, Z., Xiang, C., Yao, X., Floch, P.L., Mendez, J., Suo, Z., 2019. Stretchable materials of high toughness and low hysteresis. Proc. Natl. Acad. Sci. 116, 5967–5972. http://dx.doi.org/10.1073/pnas.1821420116.

Wang, L., Zheng, D., Harker, P., Patel, A.B., Guo, C.F., Zhao, X., 2021. Evolutionary design of magnetic soft continuum robots. Proc. Natl. Acad. Sci. 118, e2021922118. http://dx.doi.org/10.1073/pnas.2021922118.

Yan, D., Abbasi, A., Reis, P.M., 2021a. A comprehensive framework for hard-magnetic beams: Reduced-order theory, 3D simulations, and experiments. Int. J. Solids Struct. 111319, http://dx.doi.org/10.1016/j.ijsolstr.2021.111319, https://www.sciencedirect.com/science/article/pii/S0020768321003978.

Yan, D., Pezzulla, M., Cruveiller, L., Abbasi, A., Reis, P.M., 2021b. Magneto-active elastic shells with tunable buckling strength, 12. http://dx.doi.org/10.1038/s41467-021-22776-y.

Yih-Hsing, P., Chau-Shioung, Y., 1973. A linear theory for soft ferromagnetic elastic solids. Internat. J. Engrg. Sci. 11, 415–436. http://dx.doi.org/10.1016/0020-7225(73)90059-1, https://www.sciencedirect.com/science/article/pii/0020722573900591.

Zhao, R., Kim, Y., Chester, S.A., Sharma, P., Zhao, X., 2019. Mechanics of hard-magnetic soft materials. J. Mech. Phys. Solids 124, 244–263. http://dx.doi.org/10.1016/j.jmps.2018.10.008.

Zhou, R., Surendran, A.N., Mejulu, M., Lin, Y., 2020. Rapid microfluidic mixer based on ferrofluid and integrated microscale NdFeB-PDMS magnet. Micromachines 11 (29), http://dx.doi.org/10.3390/mi11010029.